A spectral/hp element depth-integrated model for nonlinear wave-body interaction

Umberto Bosi, Allan Peter P Engsig-Karup, Claes Eskilsson, Mario Ricchiuto

A spectral/*hp* element depth-integrated model for nonlinear wave-body interaction

U. Bosi, A.P. Engsig-Karup, C. Eskilsson, M. Ricchiuto

RESEARCH REPORT
N° 9166
April 2018
Project-Team Cardamom

ISSN 0249-6399 ISRN INRIA/RR--9166--FR+ENG

A spectral/*hp* element depth-integrated model for nonlinear wave-body interaction

U. Bosi*, A.P. Engsig-Karup†, C. Eskilsson‡, M. Ricchiuto*

Project-Team Cardamom

Research Report n° 9166 — April 2018 — 35 pages

Abstract: We present a spectral/*hp* element method for a depth-integrated Boussinsq model for the efficient simulation of nonlinear wave-body interaction. The model exploits a 'unified' Boussinesq framework, i.e. the flow under the body is also treated with the depth-integrated approach, initially proposed by Jiang [25] and more recently rigorously analysed by Lannes [28]. The choice of the Boussinesq equations allows the elimination of the vertical dimension, resulting in a wave-body model with an adequate precision for weakly nonlinear and dispersive waves expressed in horizontal dimensions only. The framework involves the coupling of two different domains with different flow characteristics. In this work we employ flux-based conditions for domain coupling, following the recipes provided by the discontinuous Galerkin spectral/*hp* element framework. Inside each domain, the continuous spectral/*hp* element method is used to solve the appropriate flow model. The spectral/*hp* element method allows to achieve high-order, possibly exponential, convergence for non-breaking waves, and account for the nonlinear interaction with fixed and floating bodies. Our main contribution is to include floating surface-piercing bodies in the conventional depth-integrated Boussinesq framework and the use of a spectral/*hp* element method for high-order accurate numerical discretization in space. The model is validated against published results for wave-body interaction and confirmed to have excellent accuracy. The proposed nonlinear model is demonstrated to be relevant for the simulation of wave energy devices.

Key-words: nonlinear and dispersive waves, wave-body interaction, Boussinesq equations, spectral/*hp* element method, discontinuous Galerkin method, domain decomposition

* Inria BSO, Team Cardamom
† Technical University of Denmark
‡ RISE (Sweden) and University of Aalborg (Denmark)

RESEARCH CENTRE
BORDEAUX – SUD-OUEST

200, Avenue de la Vieille Tour
33405 Talence Cedex

Une approache spectral/*hp* element moyenne sur la profondeur pour l'interaction vagues-structure

Résumé : Nous présentons une méthode éléments finis spectral pour un modèle de Boussinsq intégré sur la profondeur pour la simulation efficace de l'interaction non-linéaire vagues-structures. Le modèle exploite un cadre Boussinesq unifié, c'est-à-dire que lécoulement sous le corps est également traité avec l'approche intégrée en profondeur, initialement proposar (Jiang, 2001) et plus récemment rigoureusement analysée par (Lannes, 2016). Le choix des équations de Boussinesq permet l'élimination de la dimension verticale, aboutissant à un modèle avec une précision adéquate pour les ondes non linéaires et faiblement dispersives représentées uniquement avec en termes de dimensions horizontales. Le cadre implique le couplage de deux domaines différents avec des caractéristiques d'écoulement diférentes. Dans ce travail, nous utilisons des conditions de couplage basées sur les flux, en suivant les recettes typique des méthodes éléments finis discontinus. A l'intérieur de chaque domaine, la méthode spectrale continue est utilisée pour résoudre le modèle approprié. Cette approche permet d'obtenir une convergence d'ordre élevé, éventuellement exponentielle, pour les ondes non déferlantes, et de prendre en compte l'interaction non linéaire avec des corps fixes et flottants. Notre contribution principale consiste à inclure des corps flottants dans le cadre conventionnel de Boussinesq, combinant cela avec l'approche éléments finis spectral. Le modèle est validé sur des cas classiques d'interaction vagues-structures et confirmé avoir une excellente précision. On montre aussi que cette approche est pertinente pour la simulation de dispositifs re recuperation de l'énergie de la houle.

Mots-clés : vagues non-linéaires, interaction vagues-structure, modèles Boussinesq, éléments finis

1 Introduction

Wave models based on depth-integrated Boussinesq-type wave equations [37, 2, 32] are standard engineering tools for simulating nonlinear wave propagation and transformation in coastal areas. Boussinesq-type models are computationally efficient due to the elimination of the vertical dimension of the problem, as well as avoiding the problem of a time-dependent computational domain since the moving free surface boundary condition. However, the nature of the depth-integrated approach gives that truncated surface-piercing bodies are troublesome to handle. In order to include truncated bodies in depth-integrated hydrodynamic models, methods such as pressure patches [17], porosity layers [35] and slender ship approximations [7] have been used. None of these approaches includes the actual body in the discretization. The exception is the work of Jiang [25] on the 'unified' Boussinesq model. Jiang decomposed the domain into a free-surface domain and a body domain. Importantly, Jiang modelled also the domain under the body with a depth-integrated approach – hence the term 'unified'. A similar setting was recently rigorously analyzed by Lannes [28]. Lannes extended the work of John [26] to include nonlinear contributions and derived semi-analytic nonlinear solutions for the wave-body problem using the nonlinear shallow water equations. However, the study of Lannes mainly kept within the traditional shallow water limit.

In this study we propose a depth-integrated unified Boussinesq model for nonlinear wave-body interaction based on the approach introduced by Jiang [25]. Adapting the original idea in terms of governing equations and discretizations, we employ a spectral/*hp* finite element method for the simulation of nonlinear and dispersive waves interacting with fixed and heaving bodies. In particular, we employ the continuous spectral/*hp* element method [27] inside each domain, and implement flux-based coupling conditions between domains in line with the discontinuous Galerkin spectral/*hp* element method [8]. This results in a new efficient and accurate model that simulates the wave propagation and the nonlinear interaction of waves with bodies. However, as all models based on Boussinesq-type equations, the model is limited to the shallow and intermediate depth regimes. High-order finite element methods for depth-integrated wave models have been presented in [20, 21, 15, 13, 11, 40].

The present study presents the underlying formulation of the method as well as verification and validation of the numerical model. Although the model is not limited to applications in marine renewable energy, the reason for developing a medium fidelity wave-body model is found in the present state of modelling wave energy converters (WECs). Today the industry standard description of the interaction between waves and WECs is based on models solving the Cummins equation [9] using hydrodynamic coefficients computed from linear potential flow. The linear models are used for their simplicity and efficiency, e.g. see [33]. The linear models, however, cannot account for nonlinear hydrodynamic effects which are of importance especially for survival cases as well as for WECs operating inside the resonance region. The linear models overpredict the power production in the resonance region unless drag coefficients are calibrated. Moreover, WEC farms are initially planned to be placed in nearshore regions where is unlikely to have a flat seabed and waves present nonlinear dynamics, as steepening and energy transfer between harmonics. More recently, Reynolds Averaged Navier-Stokes (RANS) simulations have been employed for point absorber WECs, e.g. [43, 36, 3]. RANS is a complete and accurate model with respect to nonlinear phenomena but computationally very costly. For example, a simulation with a full sea state for a WEC may require as much as 150 000 CPU hours per simulation [19]. At present RANS models are therefore unsuited for the optimisation of single devices, not to mention energy farms. In shallow to intermediate waters, Boussinesq-type models as the one proposed here, are an intermediate way between the efficient but too simple linear model and the complete but too expensive RANS model.

The paper, which expands and improves the concepts introduced in [18], is structured as follows. We present three hydrodynamic long wave models that are useful to asses the developed framework in section 2: the nonlinear shallow water equations (NSW), the Abbott equations [1] and the Madsen and Sørensen equations (MS) [32]. The new numerical spectral/*hp* element scheme is described in sections 3, where we show the time and space discretization and the numerical results obtained that verified the accuracy of the framework. In particular we discuss the coupling between free surface models, and wave-body coupling and their convergence (sections 4.1 and 4.3). The use of a spectral/*hp* element discretization scheme gives support for the use of adaptive meshes for geometric flexibility, such that different grids can be used in the free surface domain and in the body domain, and high-order accurate approximations that help make the scheme efficient. The model is validated against test cases found in literature in sections 4.4 – 4.6. A heaving box test is presented in section 5 and the results from the Boussinesq model is compared to linear as well as RANS simulations. A proof-of-concept highlighting the flexibility of the framework with multiple bodies interacting with weakly nonlinear incoming waves is demonstrated in section 6. Finally, the paper is summarized and discussed in section 7.

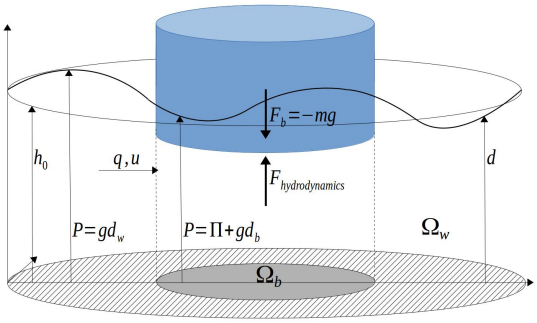

Figure 1: Layout of the problem describing the nonlinear wave-body interaction in a domain decomposition framework.

2 Hydrodynamic Model

We present here the governing models that will solve the nonlinear wave-body interaction problem, in particular the NSW model, the Abbott model and the MS model. In this work we limit ourselves to straight-sided body interfaces that are assumed vertical at the wave-body intersection. Also, only heaving movement is considered for the moment. The shallow water approximation is relevant only for very long waves and, in general, when the dispersion parameter κh_0 is less than $\approx \frac{\pi}{20}$, with κ the wavenumber and h_0 the still water depth. To account for the dispersive effects taking place for shorter waves (or deeper waters), we consider Boussinesq-type models that includes weakly nonlinear and dispersive effects, thus enlarging the application window to reduced wavelengths of $\kappa h_0 \approx 0.44\pi$ (Abbott) and $\kappa h_0 \approx \pi$ (MS), respectively.

2.1 Governing equations

Shallow water and Boussinesq models for free surface flows can be derived from the fully nonlinear potential equations for an incompressible, irrotational and non-viscous fluid by expanding the velocity potential in terms of the vertical coordinate and integrating the Laplace equation over the water depth. Denoting A_0, h_0 and λ_0 as the characteristic wave amplitude, characteristic still water depth and characteristic wave length, we obtain these models from an asymptotic approximation in terms of nonlinearity ($\varepsilon = \frac{A_0}{h_0}$) and dispersion ($\mu = \frac{2\pi h_0}{\lambda_0}$). These asymptotic and depth integrated models have the advantage of reducing the problem to a lower-dimensional one ($\mathbb{R}^d \to \mathbb{R}^{d-1}$), but it comes with an application window that depends on the approximation order of nonlinearity and dispersion assumed in the Boussinesq derivation procedure [31].

In the unified approach proposed, we divide the domain in an outer free surface subdomain Ω_w and a inner subdomain Ω_b that represents the area under the structure, as shown in figure 1.

In the simple case of fully hydrostatic approximation with constant bathymetry, the model equations are [25, 28]

$$d_t + \nabla \cdot \boldsymbol{q} = 0\,, \tag{1a}$$

$$\boldsymbol{q}_t + \nabla \cdot (\boldsymbol{u} \otimes \boldsymbol{q}) + d\nabla\,(gd + \Pi) = 0\,, \tag{1b}$$

where the variables $d(\boldsymbol{x}, t), \boldsymbol{u}(\boldsymbol{x}, t)$ and $\boldsymbol{q}(\boldsymbol{x}, t)$ are the depth measured as the height of the water column, depth-averaged velocity, and the mass flux ($\boldsymbol{q} = d\boldsymbol{u}$), respectively. We have denoted with g the acceleration of gravity, and by Π the pressure at the free surface. We will refer to this case as the nonlinear shallow water (NSW) case. The model is valid both in the free surface domain Ω_w and the domain below the body Ω_b. However, in the free surface region Ω_w, Π is equal to the atmospheric pressure. It is custom to set the reference pressure above the free surface to zero. Conversely, in the inner domain Π represent the pressure on the body surface, which is a priori neither constant nor known. We introduce the definition of total pressure

$$P(\boldsymbol{x}, t) = \begin{cases} gd(\boldsymbol{x}, t)\,, & \text{if } \mathbf{x} \in \Omega_w; \\ gd(\boldsymbol{x}, t) + \Pi(\boldsymbol{x}, t)\,, & \text{if } \mathbf{x} \in \Omega_b, \end{cases} \tag{2}$$

that for the body domain can be evaluated by taking the divergence of eq. (1b)

$$-\nabla \cdot (d\nabla P) = \nabla \cdot \boldsymbol{q}_t + \nabla \cdot (\nabla \cdot (\boldsymbol{u} \otimes \boldsymbol{q})). \tag{3}$$

Introducing the vertical acceleration $a = d_{tt}$, and using the continuity eq. (1a) we have

$$a + (\nabla \cdot \boldsymbol{q})_t = 0, \tag{4}$$

and assuming that all variables are continuous, we can change the order of the space and time derivative

$$a = -\nabla \cdot (\boldsymbol{q}_t). \tag{5}$$

Combining eqs. (3) and (5), we can show that in both the inner and outer domains the total pressure satisfies the following equation

$$-\nabla \cdot (d\nabla P) = -a + \Delta \cdot (\boldsymbol{u} \otimes \boldsymbol{q}), \tag{6}$$

where Δ denotes the Laplace operator. Thus we have a set of three equations which have to be satisfied both in the free surface domain Ω_w and for the body domain Ω_b

$$d_t + \nabla \cdot \boldsymbol{q} = 0\,, \tag{7a}$$
$$\boldsymbol{q}_t + \nabla \cdot (\boldsymbol{u} \otimes \boldsymbol{q}) + d\nabla P = 0\,, \tag{7b}$$
$$-\nabla \cdot (d\nabla P) = -a + \Delta \cdot (\boldsymbol{u} \otimes \boldsymbol{q}). \tag{7c}$$

The main difference between the two domains is that in Ω_w the total pressure and the free surface elevation are readily obtained by eq. (7a), automatically satisfying eq. (7c). On the other hand, in the inner domain Ω_b, the relation (7a) acts as a constraint on the flux divergence, exactly as in incompressible flow. The total pressure is in this case determined from eq. (7c), with the satisfaction of eq. (7a) coming as a constraint. In particular, this is where the coupling with the dynamics of the structure appear. For a purely heaving body, the vertical acceleration will be determined by the application of Newton's second law to the body

$$m_b a = -m_b g + F_{hydrodynamics}\,, \tag{8}$$

where ρ_w is the water density and m_b the mass of the body. The hydrodynamic force is evaluated integrating the hydrodynamic pressure Π over the body bottom

$$F_{hydrodynamics} = \rho_w \int_{\Omega_b} \Pi d\boldsymbol{x}. \tag{9}$$

Equation (8) is added to the final NSW system to account for the movement of the body caused by the wave-body interaction.

In the non-hydrostatic case one needs to account for dispersion effects. The simplest Boussinesq-type dispersive model considered is the one due to Peregrine [37] which, assuming constant bathymetry, modifies eq. (1b) as

$$\boldsymbol{q}_t + \nabla \cdot (\boldsymbol{u} \otimes \boldsymbol{q}) + d\nabla P = d\frac{h_0^2}{3}\nabla(\nabla \cdot \boldsymbol{u}_t). \tag{10}$$

It has been shown in [22] that, within the same asymptotic accuracy w.r.t. κh_0, one can also consider the model proposed by Abbot *et al.* [1], in which eq. (1b) is replaced by

$$\boldsymbol{q}_t + \nabla \cdot (\boldsymbol{u} \otimes \boldsymbol{q}) + d\nabla P = \frac{h_0^2}{3}\nabla(\nabla \cdot \boldsymbol{q}_t). \tag{11}$$

This model constitutes the basis of the dispersion enhanced model proposed by Madsen and Sørensen (MS) [32] which can be written (assuming constant bathymetry) as

$$\boldsymbol{q}_t + \nabla \cdot (\boldsymbol{u} \otimes \boldsymbol{q}) + d\nabla P = Bh_0^2\nabla(\nabla \cdot \boldsymbol{q}_t) + \alpha_{MS}h_0^3\nabla(\Delta P). \tag{12}$$

The parameters α_{MS} and B are defined in the literature as $\alpha_{MS} = \frac{1}{15}$ and $B = \frac{1}{3} + \alpha_{MS}$ and will optimize the linear dispersion relation of the system [38]. Note that varying the two parameters we can trace back the other models presented, for $\alpha_{MS} = 0$ we have the Abbott model and for $\alpha_{MS} = B = 0$ the NSW model. In the inner domain, we can prove the following result:

Proposition 1. *Within the accuracy of the asymptotic Boussinesq expansion, and in absence of pitch, roll, and yaw all terms accounting for higher-order dispersive effects in the inner domain are negligible.*

Proof. The term $\nabla(\nabla \cdot \boldsymbol{q}_t)$ from the momentum equation is be put in relation to the body elevation through the mass equation

$$\nabla d_{tt} + \nabla(\nabla \cdot \boldsymbol{q}_t) = 0, \tag{13}$$

but $\nabla d_{tt} = 0$ as it is the derivative of a constant value in space. Thus, under the hypothesis made, the dispersion term is zero. To demonstrate that the term $\nabla(\Delta P) = 0$ consider the non dimensional variables $\tilde{\boldsymbol{q}}, \tilde{P}$ and $\tilde{d}$, presented in A. We now repeat the steps done for the construction of model (12). In particular, from the non-dimensional momentum equation, in the Boussinesq approximation, we know that

$$\tilde{\boldsymbol{q}}_t + \tilde{d}\nabla\tilde{P} = \mathcal{O}(\varepsilon, \mu^2), \tag{14}$$

the variable $\tilde{d} = \tilde{h}_0 + \mathcal{O}(\varepsilon)$ so we simplify eq. (14) to express it in the form

$$\tilde{\boldsymbol{q}}_t + \tilde{h}_0\nabla\tilde{P} = \mathcal{O}(\varepsilon, \mu^2). \tag{15}$$

Taking the gradient of the divergence of eq. (15)

$$\nabla(\nabla \cdot \tilde{\boldsymbol{q}})_t + \nabla(\nabla \cdot (\tilde{h}_0\nabla\tilde{P})) = \mathcal{O}(\varepsilon, \mu^2), \tag{16}$$

for a constant bathymethry, $\tilde{h}_0$ can be moved out the derivation

$$\nabla(\nabla \cdot \tilde{\boldsymbol{q}}_t) + \tilde{h}_0\nabla(\Delta\tilde{P}) = \mathcal{O}(\varepsilon, \mu^2), \tag{17}$$

but we know that $\nabla(\nabla \cdot \tilde{\boldsymbol{q}}_t) = 0$, which proves that $\nabla(\Delta\tilde{P})$ is within the asymptotic error of the model and can be considered zero in all the applications. □

The focus of this paper is a 2D wave modelled by a 1D $+z$ system of PDEs. In the outer domain, we will solve the 1D MS model in first order formulation, reading

$$P_t + gq_x = 0\,, \tag{18a}$$
$$q_t + uq_x + dP_x = D\,, \tag{18b}$$
$$D = Bh_0^2G_x + \alpha_{MS}h_0^2dF_x\,, \qquad x \in \Omega_w, \tag{18c}$$
$$G - q_{xt} = 0\,, \tag{18d}$$
$$F - N_x = 0\,, \tag{18e}$$
$$N - P_x = 0. \tag{18f}$$

where we have multiplied the mass equation (18) by g such that we can use the same set of variables (P, q), through all the domains. Rearranging the first order equations in the eq. (18b), we can define the one dimensional linear operators

$$\mathcal{L}_B(\cdot) = (1 - Bh_0^2\partial_{xx})(\cdot), \qquad \mathcal{B}_d^\alpha(\cdot) = d\partial_x(1 + \alpha_{MS}h_0^2\partial_{xx})(\cdot). \tag{19}$$

Note that the operator $\mathcal{B}_d^\alpha(\cdot)$ has also the high order component dependent on d. This is possible since the still water depth h_0 and the instant elevation d are of the same order of approximation, as we can see in appendix A, and they can be substituted one with the other. Under the body (or "inner" domain), thanks for the proposition 1, we solve the non dispersive 1D NSW system

$$q_t + (uq)_x + dP_x = 0\,, \tag{20a}$$
$$-w_x = -a + k_x\,, \qquad x \in \Omega_b, \tag{20b}$$
$$w - dP_x = 0\,, \tag{20c}$$
$$k - (qu)_x = 0. \tag{20d}$$

As for eq. (7), in eq. (18) we solve eq. (18a) and eq. (18b), while in eq (20) we solve eqs. (20a) and (20b). Note that the 1D mass equation is valid also in the inner domain, but is not solved and is implicit in eq. (20b). Unfortunately, the transmission conditions between the dispersive outer domain and the non dispersive inner domain cannot be rigorously formulated in the nonlinear case [28, 29] and we have decided to handle them numerically. We do this introducing a small NSW transition layer Ω_l on the sides of the body, where we solve

$$P_t + gq_x = 0\,, \qquad x \in \Omega_l, \tag{21a}$$
$$q_t + (uq)_x + dP_x = 0. \tag{21b}$$

The stability and accuracy of the dispersive/hydrostatic coupling is investigated thoroughly in the result section 4.

2.2 Boundary condition and interfaces coupling condition

The three sets of shallow water equations, describing the two free surface domain (18), (21) and the inner domain (20) are coupled through the mass flux $\boldsymbol{q}$ and the total pressure P. At the interface between the body and free surface domains, $(x_{li}, y_{li}) \in \Omega_l \cap \Omega_b$ the coupling conditions at the waterline read

$$\boldsymbol{q}_l(x_{li}, y_{li}) = \boldsymbol{q}_b(x_{li}, y_{li}), \tag{22}$$

$$P_l(x_{li}, y_{li}) = P_b(x_{li}, y_{li}). \tag{23}$$

where $(\boldsymbol{q}_l, P_l) \in \Omega_l$ and $(\boldsymbol{q}_b, P_b) \in \Omega_b$. Note that the pressure coupling condition (23) can be expanded and written also as

$$gd_l(x_{li}, y_{li}) = gd_b(x_{li}, y_{li}) + \Pi_b(x_{li}, y_{li}). \tag{24}$$

In the coupling two free surface domains, at $(x_{wl}, y_{wl}) \in \Omega_w \cap \Omega_l$, $\Pi(x_{wl}, y_{wl})$ is zero and the condition states that the wave elevation and the flow must be equal through the interface

$$\begin{aligned} d_w(x_{wi}, y_{wi}) &= d_l(x_{wl}, y_{wl}), \\ q_w(x_{wl}, y_{wl}) &= q_l(x_{wl}, y_{wl}). \end{aligned} \tag{25}$$

On the external boundaries of the outer domains (on the far field), we impose the absorption of the wave, thus

$$\begin{aligned} d_w|_{\pm\infty} &= h_0, \\ \boldsymbol{q}_w|_{\pm\infty} &= 0. \end{aligned} \tag{26}$$

3 Numerical Model

3.1 Spatial Discretization

Consider the the domain Ω, which can represent the any of the domains presented, and a test function φ defined in the discrete space $\mathcal{V}^P$

$$\mathcal{V}^p = \left\{ \varphi_i \in L^2(\Omega) : \varphi_i|_\Omega \in \mathcal{P}^p \right\}, \tag{27}$$

where $\mathcal{P}^p$ is the space of polynomials of degree at most p. We propose a spectral/hp element approach to discretize in space the models presented in section 2. Following a DG-FEM type recipe based on double integration by parts on each sub-domain [10, 23], we multiply the eqs. (18), (20) and (21) by φ and integrate in each domain to obtain the weak form. However, the systems present non-conservative products, namely the dP_x terms, which are not continuous over the boundaries from the free surface domains to the body one. Using an approach similar to the one suggested in [10, 6, 34], we treat these products by introducing in the variational statements penalty terms consistent with a local linearization of the quasi-linear form of the system:

$$\int_{\Omega_w} \varphi_i P_t dx + g \int_{\Omega_w} \varphi_i q_x dx + g \int_{\partial\Omega_w} \varphi_i [q] \boldsymbol{n} dx = 0, \tag{28a}$$

$$\int_{\Omega_w} \varphi_i q_t dx + \int_{\Omega_w} \varphi_i (qu)_x dx + \int_{\partial\Omega_w} \varphi_i [qu] \boldsymbol{n} dx + \int_{\Omega_w} \varphi_i dP_x dx + \int_{\partial\Omega_w} \varphi_i \langle d \rangle [P] \boldsymbol{n} dx = \int_{\Omega_w} \varphi_i D dx, \tag{28b}$$

$$\int_{\Omega_w} \varphi_i D dx = B h_0^2 \left(\int_{\Omega_w} \varphi_i G_x dx + \int_{\partial\Omega_w} \varphi_i [G] \boldsymbol{n} dx \right) + \alpha_{MS} h_0^2 \left(\int_{\Omega_w} \varphi_i dF_x dx + \int_{\partial\Omega_w} \varphi_i \langle d \rangle [F] \boldsymbol{n} dx \right), \tag{28c}$$

$$\int_{\Omega_w} \varphi_i G dx - \int_{\Omega_w} \varphi_i q_{xt} - \int_{\partial\Omega_w} \varphi_i [q_t] \boldsymbol{n} dx = 0, \tag{28d}$$

$$\int_{\Omega_w} \varphi F - \int_{\Omega_w} \varphi_i N_x - \int_{\partial\Omega_w} \varphi_i [N] \boldsymbol{n} dx = 0, \tag{28e}$$

$$\int_{\Omega_w} \varphi_i N - \int_{\Omega_w} \varphi_i P_x - \int_{\partial\Omega_w} \varphi_i [P] \boldsymbol{n} dx = 0. \tag{28f}$$

where $\boldsymbol{n}$ represents the outward pointing normal vector. In general, the integral boundary terms are in the form

$$[u] = \hat{u} - u^- \tag{29}$$

where $\hat{u}$ represent a numerical flux through the boundary interface and u^- the value of the function on the boundary for x inside the domain. Note that, the numerical flux between the domains, often is based on an approximate Riemann solver for the advective parts [20] and a LDG type [42] or hybridizeable DG [40] for the higher-order terms. Here we have used simple central fluxes

$$\hat{u} = \frac{1}{2}\left(u^+ + u^-\right). \tag{30}$$

Substituting in eq. (29), we obtain the jumps between the domains for first derivative terms

$$[u] = \frac{1}{2}\left(u^+ - u^-\right), \tag{31}$$

where u^+ is the values on the boundary in the neighbor domain. The coefficient multiplying non conservative terms is treated taking the average value of the depth on the two side of the boundary

$$\langle d \rangle = \frac{d^+ + d^-}{2}. \tag{32}$$

This simple choice allows to recover the conservative form in the hydrostatic free surface region, as we have exactly that

$$\langle d \rangle [d] = \frac{\hat{d}^2}{2} - \left(\frac{d^2}{2}\right)^-. \tag{33}$$

In the same manner, the weak formulation in the body and the NSW domain is

$$\int_{\Omega_b} \varphi_i q_t dx + \int_{\Omega_b} \varphi_i (qu)_x dx + \int_{\partial\Omega_b} \varphi_i [qu] \boldsymbol{n} dx + \int_{\Omega_b} \varphi_i dP_x dx + \int_{\partial\Omega_b} \varphi_i \langle d \rangle [P] \boldsymbol{n} dx = 0, \tag{34a}$$

$$-\int_{\Omega_b} \varphi_i w_x dx \int_{\partial\Omega_b} \varphi_i [w] \boldsymbol{n} dx = -\int_{\Omega_b} \varphi_i a dx + \int_{\Omega_b} \varphi_i k_x dx \int_{\partial\Omega_b} \varphi_i [k] \boldsymbol{n} dx, \tag{34b}$$

$$\int_{\Omega_b} \varphi_i w - \int_{\Omega_b} \varphi_i dP_x - \int_{\partial\Omega_b} \varphi_i \langle d \rangle [k] \boldsymbol{n} dx = 0, \tag{34c}$$

$$\int_{\Omega_b} \varphi_i k - \int_{\Omega_b} \varphi_i (qu)_x - \int_{\partial\Omega_b} \varphi_i [qu] \boldsymbol{n} dx = 0. \tag{34d}$$

$$\int_{\Omega_l} \varphi_i P_t dx + g \int_{\Omega_l} \varphi_i q_x dx + g \int_{\partial\Omega_l} \varphi_i [q] \boldsymbol{n} dx = 0, \tag{35a}$$

$$\int_{\Omega_l} \varphi_i q_t dx + \int_{\Omega_l} \varphi_i (qu)_x dx + \int_{\partial\Omega_l} \varphi_i [qu] \boldsymbol{n} dx + \int_{\Omega_l} \varphi_i dP_x dx + \int_{\partial\Omega_l} \varphi_i \langle d \rangle [P] \boldsymbol{n} dx = 0. \tag{35b}$$

Proposition 2. *Defined the hydrostatic steady state of the system as*

$$(\bar{d}_{w,l}, \bar{d}_b(x), \bar{P}, \bar{q}, \bar{u}) = (h_0, d_b(x), g h_0, 0, 0), \tag{36}$$

where h_0 is the still water depth and $d_b(x)$ is the depth corresponding to the geometry of the body at rest when the volume of water displaced by the body is equal to the mass of the body over ρ_w

$$\frac{m_b}{\rho_w} = \int_{\Omega_b} (h_0 - \bar{d}_b(x)). \tag{37}$$

The variational formulation is well balanced: the hydrostatic steady state (36) is an exact solution of the weak form.

Proof. The definition of the steady state is true, in particular the total pressure P can be shown to be constant from eq. (2). In the NSW case, the hydrostatic pressure $\bar{\Pi}$ in the steady state can be found dividing by the depth $\bar{d}_b(x)$ and integrating over Ω_b the eq. (20b)

$$\bar{\Pi}(x) = g(h_0 - \bar{d}_b(x)) + \int_\Omega \frac{1}{\bar{d}_b(x)} (\bar{q}_t + (\bar{q}\bar{u})_x) dx, \quad x \in \Omega_b, \tag{38}$$

but $\bar{q} = 0$. Thus we know that the hydrostatic pressure in the inner domain results in

$$\bar{\Pi}(x) = g(h_0 - \bar{d}_b(x)), \quad x \in \Omega_b, \tag{39}$$

because $u = \frac{\bar{q}^2}{d_b} = 0$. We can demonstrate that the total pressure P is constant

$$\bar{P} = \begin{cases} gh_0\,, & \text{if } \mathbf{x} \in \Omega_w; \\ g\bar{d}_b(x) + \bar{\Pi}(x) = gh_0\,, & \text{if } \mathbf{x} \in \Omega_b. \end{cases} \tag{40}$$

The momentum equations

$$\int_{\Omega_\gamma} \varphi q_t dx + \int \varphi_{\Omega_\gamma}(qu)_x dx + \int_{\partial\Omega_\gamma} \varphi[qu]\boldsymbol{n}dx + \int_{\Omega_\gamma} \varphi dP_x dx + \int_{\partial\Omega_\gamma} \varphi\langle d\rangle[P]\boldsymbol{n}dx = \int_{\Omega_\gamma} \varphi q_t dx = 0 \tag{41}$$

because the total pressure is constant, $P_x = 0$ and because of eq. (40) also the jump $[P] = 0$. It can be shown that the acceleration of the body is also zero. From eq. (2) and eq. (9)

$$m_b a = -m_b g + \rho_w \int_{\Omega_b} (\bar{P} - g\bar{d}_b(x))dx, \tag{42}$$

using eq. (40)

$$\rho_w \int_{\Omega_b} (\bar{P} - gd(x))dx = g\rho_w \int_{\Omega_b} (h_0 - \bar{d}_b(x))dx, \tag{43}$$

but the integral $\int_{\Omega_b}(h_0 - \bar{d}_b(x))$ is the volume of water displaced by the body and at the steady state as in eq. (37), thus the acceleration is zero.

Note that well balancing is always satisfied between the MS domain and the NSW layer since all the variables involved are continuous over the boundary between the two domains. □

To obtain a fully discrete model, we now replace the unknowns with a spectral/*hp* element approximation spanned by high-order polynomial basis functions ψ_j

$$u(x,t) = \sum_{j=0}^{N_{dof}} \psi_j(x)\tilde{u}_j(t), \tag{44}$$

$\tilde{u}_j(t)$ set of interpolated function values of the solution u in the domain Ω_γ and N_{dof} the number of degree of freedom in the domain considered. Following the standard Galerkin formulation the test function and the interpolation polynomial are the same, i.e. $\varphi \in \text{span}\{\psi_j\}$. In this study we use the abscissas ot the Gauss Legendre Lobatto quadrature rule to define the nodal Lagrange polynomials [27]. This choice of basis functions gives that $\tilde{u}_j(t)$ represents the physical values at the nodal points and we therefore disregard the tilde notation in the following. We introduce then the mass and differentiation matrices, defined as

$$\boldsymbol{M}_{ij} \equiv \int_{\Omega_\gamma} \psi_i\psi_j dx, \tag{45a}$$

$$\boldsymbol{Q}_{ij} \equiv \int_{\Omega_\gamma} \psi_i(\psi_j)_x dx + 0.5\left(\psi_1\psi_1|_{\in\Omega_\gamma} - \psi_1\psi_N|_{\in\Omega_{\gamma-1}}\right) - 0.5\left(\psi_N\psi_N|_{\in\Omega_\gamma} - \psi_N\psi_1|_{\in\Omega_{\gamma+1}}\right), \tag{45b}$$

$$\tilde{\boldsymbol{Q}}_{ij} \equiv \int_{\Omega_\gamma} \psi_i d_j(\psi_j)_x dx + 0.5\langle d\rangle_{\gamma-1,\gamma}\left(\psi_1\psi_1|_{\in\Omega_\gamma} - \psi_1\psi_N|_{\in\Omega_{\gamma-1}}\right) - 0.5\langle d\rangle_{\gamma,\gamma+1}\left(\psi_N\psi_N|_{\in\Omega_\gamma} - \psi_N\psi_1|_{\in\Omega_{\gamma+1}}\right), \tag{45c}$$

having defined Ω_γ the domain of interest, $\Omega_{\gamma\pm1}$ the domains at its right and left. The weak formulation (28), (34) and (35) can be written in vector matrix formulation as

$$\boldsymbol{M}_w P_t + g\boldsymbol{Q}_w q = 0, \tag{46a}$$

$$\boldsymbol{M}_w q_t + \boldsymbol{Q}_w(qu) + \tilde{\boldsymbol{Q}}_w P = \boldsymbol{M}_w D, \tag{46b}$$

$$\boldsymbol{M}_w D = Bh_0^2\boldsymbol{Q}_w G + \alpha_{MS}h_0^2\tilde{\boldsymbol{Q}}_w F, \tag{46c}$$

$$\boldsymbol{M}_w G - \boldsymbol{Q}_w q_t = 0, \tag{46d}$$

$$\boldsymbol{M}_w F - \boldsymbol{Q}_w N = 0, \tag{46e}$$

$$\boldsymbol{M}_w N - \boldsymbol{Q}_w P = 0. \tag{46f}$$

$$\boldsymbol{M}_b q_t + \boldsymbol{Q}_b(qu) + \tilde{\boldsymbol{Q}}_b P = 0, \tag{47a}$$
$$-\boldsymbol{Q}_b w = -\boldsymbol{M}_b \mathbb{1} a + \boldsymbol{Q}_b k, \tag{47b}$$
$$\boldsymbol{M}_b w - \tilde{\boldsymbol{Q}}_b P = 0, \tag{47c}$$
$$\boldsymbol{M}_b k - \boldsymbol{Q}_b(qu) = 0. \tag{47d}$$

$$\boldsymbol{M}_l P_t + g\boldsymbol{Q}_l q = 0, \tag{48a}$$
$$\boldsymbol{Q}_l q_t + \boldsymbol{Q}_l(qu) + \tilde{\boldsymbol{Q}}_l P = 0. \tag{48b}$$

where $\mathbb{1}$, in eq. (47b), represents a vector of ones as the acceleration is a scalar variable. The subscripts $\{w, l, b\}$ stand for the fact that the matrices are defined in the domains Ω_w, Ω_l and Ω_b. Solving the first order equations and re-arranging the eqs. (46), (47) and (48), we define the semi-discrete formulation

$$\boldsymbol{M}_{w,l} P_t + g\boldsymbol{Q}_{w,l} q = 0\,, \qquad x \in \Omega_w \cup \Omega_l, \tag{49a}$$
$$\boldsymbol{L}_B q_t + \boldsymbol{Q}_w(uq) + \boldsymbol{B}_d^{\alpha} P = 0\,, \qquad x \in \Omega_w, \tag{49b}$$
$$\boldsymbol{M}_{l,b} q_t + \boldsymbol{Q}_{l,b}(uq) + \tilde{\boldsymbol{Q}}_{l,b} P = 0\,, \qquad x \in \Omega_l \cup \Omega_b, \tag{49c}$$
$$-\boldsymbol{Q}_b \boldsymbol{M}_b^{-1} \tilde{\boldsymbol{Q}}_b P = -\boldsymbol{M}_b \mathbb{1} a + \boldsymbol{Q}_b \boldsymbol{M}_b^{-1} \boldsymbol{Q}_b(uq)\,, \qquad x \in \Omega_b. \tag{49d}$$

We can define the global discrete linear operator

$$\boldsymbol{L}_B = \boldsymbol{M}_w - B h_0^2 \boldsymbol{Q}_w \boldsymbol{M}_w^{-1} \boldsymbol{Q}_b, \qquad \boldsymbol{B}_d^{\alpha} = \tilde{\boldsymbol{Q}}_w + \alpha_{MS} h_0^2 \tilde{\boldsymbol{Q}}_w \boldsymbol{M}_w^{-1} (\boldsymbol{Q}_w \boldsymbol{M}_w^{-1} \boldsymbol{Q}_w). \tag{50}$$

Proposition 3. *The discrete variational form (46)-(48) is well balanced: the steady hydrostatic equilibrium in eq. (36) with $\bar{a} = a = 0$, is exactly preserved.*

Proof. All the eqs. (46)-(48) are verified when we substitute the steady hydrostatic equilibrium as solution of the scheme. □

Remark 1. *The total pressure P verifies the same discrete equation in all domains. In fact, eq. (49d) is a consequence of the semi-discrete mass equation (49a) solved in the free surface domains. In the inner domain Ω_b, the satisfaction of the mass equation $\boldsymbol{M}_b d_t + \boldsymbol{Q}_b q = 0$ is obtained by imposing it implicitly as a constrain. This provides an exact discrete consistency between the mass and pressure equations in all domains.*

3.2 Time Discretization

For the time discretization we substitute the variables with their time discrete correspondent. In this paper is implemented an extrapolated backward differentiation formula of third order (eBDF3). This method is of order three in time, guarantees a fast convergence and an error always smaller than the error in space, making it ideal for the convergence study with a manufactured solution. Also it has the same computational cost of the Euler time integration. Thus, the eBFD3 with spectral/*hp* elements method results in a very efficient method in time and space to solve our wave-body interaction problem. Introducing the notation $q^n = q(x, t^n)$, the time derivative for eBDF3 time integration is expressed as

$$\delta q = \frac{11q^{n+1} - 18q^n + 9q^{n-1} - 2q^{n-2}}{6\delta t}, \tag{51}$$

for constant time steps δt. The nonlinear term are evaluated at time $n+1$ by a linear extrapolation. This extrapolation is

$$q^e = 3q^n - 3q^{n-1} + q^{n-2}. \tag{52}$$

The time-step δt is chosen in relation with the mesh dimension δx through a standard CFL condition [14]. For the grid convergence studies δt is appropriately reduced such that the error in time is always dominated by the error in space. Finally, the model (49) discretized in time and space

$$\boldsymbol{M}_{w,l} \delta P + g\boldsymbol{Q}_{w,l} q = 0\,, \qquad x \in \Omega_w \cup \Omega_l, \tag{53a}$$
$$\boldsymbol{L}_B \delta q + \boldsymbol{Q}_w(uq) + \boldsymbol{B}_d^{\alpha} P = 0\,, \qquad x \in \Omega_w, \tag{53b}$$
$$\boldsymbol{M}_{l,b} \delta q + \boldsymbol{Q}_{l,b}(uq) + \tilde{\boldsymbol{Q}}_{l,b} P = 0\,, \qquad x \in \Omega_l \cup \Omega_b, \tag{53c}$$
$$-\boldsymbol{Q}_b \boldsymbol{M}_b^{-1} \tilde{\boldsymbol{Q}}_b P = -\boldsymbol{M}_b \mathbb{1} a + \boldsymbol{Q}_b \boldsymbol{M}_b^{-1} \boldsymbol{Q}_b(uq)\,, \qquad x \in \Omega_b. \tag{53d}$$

Note that the linear operator $\boldsymbol{B}_d^\alpha$ is evaluated with the extrapolated depth d. In the case of a moving body, only in the inner domain Ω_b, the acceleration is defined by Newton's second law

$$m_b a^{n+1} = -m_b g + \rho_w \int_{\Omega_b} \Pi^{n+1} dx. \tag{54}$$

We define the vector $\boldsymbol{w}$ of the Gauss-Lobatto-Legendre integration weights using the corresponding abscissas of the quadrature

$$w_i = \int_{\Omega_b} \psi_i. \tag{55}$$

So we pass to the discrete formulation

$$m_b a^{n+1} = -m_b g + \rho_w \boldsymbol{w}^T \Pi^{n+1}. \tag{56}$$

Proposition 4. *Provided that the matrix $-\boldsymbol{Q}_b \boldsymbol{M}_b^{-1} \tilde{\boldsymbol{Q}}_b$ is invertible, the dynamics of the body can be pre-computed from the fully explicit update*

$$\left(m_b + \mathcal{M}_{add}\right) a^{n+1} = -m_b g - \boldsymbol{w}^T \left(\boldsymbol{Q}_b \boldsymbol{M}_b^{-1} \tilde{\boldsymbol{Q}}_b\right)^{-1} \left(\boldsymbol{Q}_b \boldsymbol{M}_b^{-1} \boldsymbol{Q}_b (uq)^e + g \boldsymbol{Q}_b \boldsymbol{M}_b^{-1} \tilde{\boldsymbol{Q}}_b d^e\right), \tag{57}$$

where we have defined the added mass $\mathcal{M}_{add}$

$$\mathcal{M}_{add} = -\boldsymbol{w}^T \left(\boldsymbol{Q}_b \boldsymbol{M}_b^{-1} \tilde{\boldsymbol{Q}}_b\right)^{-1} \boldsymbol{w}. \tag{58}$$

Moreover, in case of constant depth, i.e. $d(x) = h$ and $\tilde{\boldsymbol{Q}}_b = h\boldsymbol{Q}_b$, it can be shown that the matrix $\boldsymbol{Q}_b M_b^{-1} \boldsymbol{Q}_b$ is positive semi-definite (PSD) and thus the added mass is nonnegative

$$\mathcal{M}_{add} \geq 0 \tag{59}$$

Proof. Solving the eq. (53d), we have a definition for the pressure that we can substitute in the acceleration eq. (54)

$$m_b a^{n+1} = -m_b g + \boldsymbol{w}^T \left(\boldsymbol{Q}_B \boldsymbol{M}_b^{-1} \tilde{\boldsymbol{Q}}_b\right)^{-1} \left(\boldsymbol{M}_b \mathbb{1} a^{n+1} - \boldsymbol{Q}_b \boldsymbol{M}_b^{-1} \boldsymbol{Q}_b (uq)^e - g \boldsymbol{Q}_b \boldsymbol{M}_b^{-1} \tilde{\boldsymbol{Q}}_b d^e\right). \tag{60}$$

Note that $\boldsymbol{M}_b \mathbb{1} a^{n+1} = \boldsymbol{w} a^{n+1}$, in fact

$$\left[\boldsymbol{M}_b \mathbb{1}\right]_i = \int_{\Omega_b} \sum_j^{N_{dof}} \psi_i \psi_j 1, \tag{61}$$

from the consistency with constant, we get for any basis function (and in particulars ours)

$$\sum_j^{N_{dof}} \psi_j = 1. \tag{62}$$

As a consequence

$$\left[\boldsymbol{M}_b \mathbb{1}\right]_i = \left(\int_{\Omega_b} \psi_i\right) 1, \tag{63}$$

and by analogy with the notation used for the pressure integral in eq. (56)

$$\left[\boldsymbol{M}_b \mathbb{1}\right]_i = w_i. \tag{64}$$

We define the resulting term, in eq. (58), added mass $\mathcal{M}_{add}$ as it is a scalar and has the dimension of a mass. Collecting the acceleration, we have the expression for the dynamics of the body eq. (57).

To show that the added mass is always non-negative for constant depth, consider the quadratic function $-\boldsymbol{w}^T \boldsymbol{Q}_b \boldsymbol{M}_b^{-1} \boldsymbol{Q}_b \boldsymbol{w}$. The mass matrix $\boldsymbol{M}_b$ is positive definite (PD) so also the inverse is PD [24]

$$\boldsymbol{M}_b > 0; \quad \boldsymbol{M}_b^{-1} > 0. \tag{65}$$

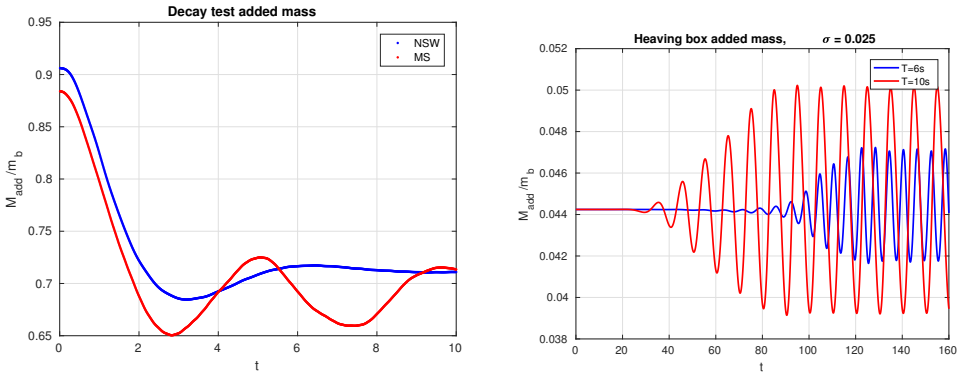

(a) (b)

Figure 2: Trends of the contribute of the added mass over the physical mass in the test presented in sections 4.6 and 5. We see that in all cases, decay movement solved with NSW and MS in figure (a) and a free heaving box with different incoming waves in (b), the value of the added mass is always positive

From eq. (45b), we can define the matrices $\boldsymbol{Q}_b$ and $\boldsymbol{Q}_b^T$

$$[\boldsymbol{Q}_b]_{ij} = \int_{\Omega_b} \psi_i (\psi_j)_x dx + 0.5 \int_{\partial\Omega_b} \psi_i \psi_j \boldsymbol{n}|_{\partial\Omega_b} dx, \tag{66a}$$

$$\left[\boldsymbol{Q}_b^T\right]_{ij} = \int_{\Omega_b} \psi_j (\psi_i)_x dx + 0.5 \int_{\partial\Omega_b} \psi_i \psi_j \boldsymbol{n}|_{\partial\Omega_b} dx. \tag{66b}$$

We also know that

$$\int_{\Omega_b} (\psi_i \psi_j)_x dx = \int_{\Omega_b} (\psi_i)_x \psi_j dx + \int_{\Omega_b} \psi_i (\psi_j)_x dx = \int_{\partial\Omega_b} \psi_i \psi_j \boldsymbol{n}|_{\partial\Omega_b} dx. \tag{67}$$

Using eq. (67) in eq. (66a), it can be shown that

$$[\boldsymbol{Q}_b]_{ij} = -\left[\boldsymbol{Q}_b^T\right]_{ij}. \tag{68}$$

Since the matrix $\boldsymbol{M}_b^{-1}$ is PD, it exist a unique PD matrix $\boldsymbol{B}$ such that $\boldsymbol{B}^2 = \boldsymbol{B}^T\boldsymbol{B} = \boldsymbol{M}_b^{-1}$ [24]. Thus, it holds the equivalence

$$-\boldsymbol{w}^T \boldsymbol{Q}_b \boldsymbol{M}_b^{-1} \boldsymbol{Q}_b \boldsymbol{w} = -\boldsymbol{w}^T \boldsymbol{Q}_b \boldsymbol{B}^T \boldsymbol{B} \boldsymbol{Q}_b \boldsymbol{w}, \tag{69}$$

but because of eq. (68), we can substitute the first $\boldsymbol{Q}_b$

$$-\boldsymbol{w}^T \boldsymbol{Q} \boldsymbol{B}^T \boldsymbol{B} \boldsymbol{Q}_b \boldsymbol{w} = \boldsymbol{w}^T \boldsymbol{Q}_b^T \boldsymbol{B}^T \boldsymbol{B} \boldsymbol{Q}_b \boldsymbol{w} = (\boldsymbol{B}\boldsymbol{Q}_b\boldsymbol{w})^T \boldsymbol{B}\boldsymbol{Q}_b\boldsymbol{w} = (\boldsymbol{B}\boldsymbol{Q}_b\boldsymbol{w})^2 \geq 0. \tag{70}$$

So $-\boldsymbol{Q}_b \boldsymbol{M}_b^{-1} \boldsymbol{Q}_b$ is PSD. When it is invertible also its inverse must be PSD [24] and the added mass is nonnegative for constant depth. □

For depth $d = d(x,t)$ we cannot demonstrate the nonnegativeness analytically. However, we have shown numerically that the added mass is always $\mathcal{M}_{add} \geq 0$ in the plots in figure 2. These show the trends of the contribute of the added mass over the real physical mass of the body in few of the tests presented in section 4, in particular the decay test with the free surface domain either solved with NSW or MS, and the free heaving test for two different incoming waves.

The strategy adopted to solve the whole problem is to evaluate at each step first the added mass $\mathcal{M}_{add}$ and the vertical acceleration of the body in eqs. (58) and (57), with the extrapolated values of the the variables from the previous time step. The updated value of the acceleration is substituted in eq. (53d), as a right hand side term, which coupled with eq. (53a) gives us $P(x, t^{n+1})$. Finally, we solve eqs. (53b) and (53c) for the updated values of the flow $q(x, t^{n+1})$. Note that all coupling conditions of the flow and elevation between outer and inner domains are accounted for by the coupling terms in the $\boldsymbol{Q}_\gamma$ and $\tilde{\boldsymbol{Q}}_\gamma$ matrices.

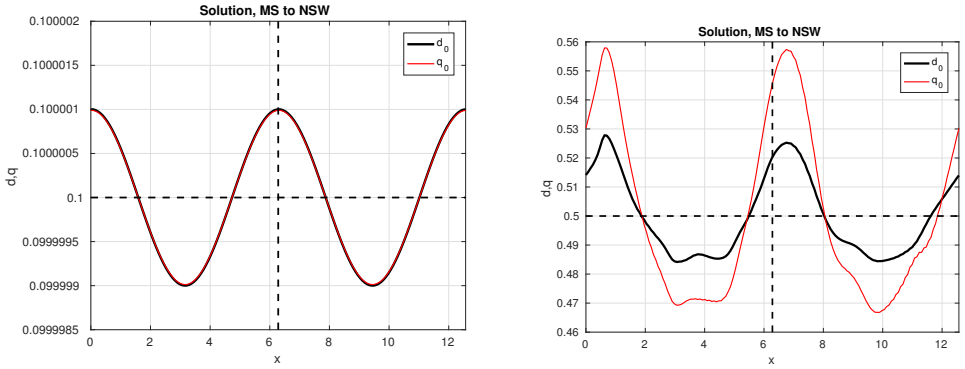

(a) (b)

Figure 3: Wave propagation tests: figure (a) shows the coupling between a MS and a NSW domain with a linear wave, with still water depth $h_0 = 0.1m$ and wave amplitude $A = 10^{-6}m$ at time $t = 25s$; figure (b) the coupling between Madsen and Sørensen and a NSW domain with a nonlinear wave, still water depth $h_0 = 0.5m$ and wave amplitude $A = 0.02m$ at time $t = 25s$. The mesh has $N_{el} = 40$ elements over each domain of 2π meters.

4 Results

The coupled approach presented in the previous sections allows to simulate waves propagating in different domains. Several combination can be considered involving free surface flow as well as floating or fixed structures. In this section, we discuss numerical results on such different combinations, whenever possible we use analytic or reference (CFD or other) solution to validate our model.

4.1 Coupling domains with different wave models

As the coupling is enforced by flux conditions that handle only the balance of incoming and outgoing flow, we can easily couple different free surface wave models. In particular, we report here the coupling between a free surface domain with MS and one with NSW. Two kind of waves are tested: a linear wave ($A = 10^{-6}m$, $h_0 = 0.1m$) and a nonlinear one ($A = 0.02m$, $h_0 = 0.5m$). The simulations are presented respectively in figures 3(a) and 3(b). The linear wave cross the different domain without alterations while the solution for the nonlinear wave shows multiple harmonics. That is due to the signal that decomposes propagating through NSW domain, as the model can not solve properly this set of waves. This test permits us to see the behaviour of the solution in particular at the coupled interfaces. As we can see from the figures, the free surface looks continuous (the jump on the interfaces is of order 10^{-13}, close to the machine precision) and no oscillation are present at the interfaces.

4.2 Grid Convergence for the free surface model

An exact solution for the MS model does not exist. The convergence of the mixed wave model is evaluated using the manufactured solution method. We consider a known function $\zeta(x - ct) = A\cos(x - ct)$, with A the wave amplitude and c the phase speed, to be imposed as the solution of the problem and evaluated the resulting equations as a Boussinesq type model with a source term.

$$\begin{aligned} P^m &= d^m(x,t) = \zeta(x-ct) + h_0, \\ u^m(x,t) &= \frac{c}{A}\zeta(x-ct), \\ q^m(x,t) &= d^m(x,t)u^m(x,t) = \frac{c}{A}\zeta(x-ct)(\zeta(x-ct)+h_0). \end{aligned} \tag{71}$$

Since it is not exact it will not satisfy the original differential equation and the substitution will result in a residual $r(\zeta) \neq 0$. This residual becomes the source term for the differential equations considered,

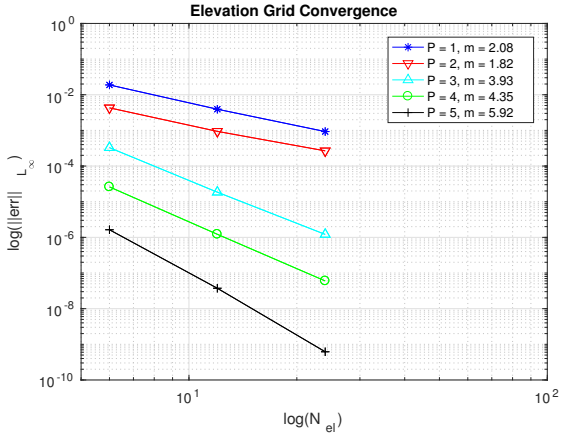

Figure 4: Convergence trend in a MS-NSW-MS model, with number of elements $N_{el} = [6, 12, 24]$ and polynomial orders $p = [1, 2, 3, 4, 5]$.

such that for NSW and MS free surface models, we have

$$\begin{aligned} &d_t + q_x = r_d(\zeta), \\ &q_t + (uq)_x + gd(P)_x = r_q^{(NSW)}(\zeta), \\ &q_t + (uq)_x + gd(P)_x - \left(\tfrac{1}{3} + \alpha_{MS}\right) h_0^2 q_{xxt} - \alpha_{MS} h_0^3 d_{xxx} = r_q^{(MS)}(\zeta). \end{aligned} \tag{72}$$

Now the function $\zeta(x-ct)$ is the exact solution of the problem and that can be compared to the numerical one for a convergence study. We had chosen $\zeta(x-ct) = A\sin(x-ct)$ since it is a simple, periodical, $\mathcal{C}^\infty(\mathbb{R} \times \mathbb{R}_+)$ function of which we can calculate all the derivative, thus the residuals $r(\zeta)$ are known exactly.

This residual terms act as source terms for the equation and are discretized in space. The discretized model is

$$\boldsymbol{A}\boldsymbol{U}_t = \boldsymbol{R}\boldsymbol{H}\boldsymbol{S} + \boldsymbol{M}\bar{r}. \tag{73}$$

The source term is evaluated exactly at time-step t_{n+1} and the initialization of the first three step necessary to eBFD3 are evaluated exactly from the manufactured solution. The convergence of the NSW and MS equations is shown in figure 4 for the meshes and orders $N_{el} = [6, 12, 24]$ and $p = [1, 2, 3, 4, 5]$. We have removed the results for $p = 5, N = 48$ as we approach the machine precision and the test is no more significant for the convergence. As we can see from the plot, we reach the optimal speed of convergence of $m = p$ for even polynomial order and $m = p + 1$ for odd ones.

4.3 Grid Convergence for a fixed inner model

We use a similar approach to test the convergence for a manufactured model with a fixed structure in the center, as in figure 6. The manufactured solution considered is

$$\begin{aligned} &P_{tot}^m = g(\zeta(x-ct) + h_0), \\ &q^m(x,t) = \frac{c}{A}\zeta(x-ct)(\zeta(x-ct) + h_0), \\ &d^m(x,t) = \begin{cases} \zeta(x-ct) + h_0\,, & \mathrm{x} \in \Omega_w, \\ h_0 - h_d\,, & \mathrm{x} \in \Omega_b. \end{cases} \end{aligned} \tag{74}$$

where h_d is the draft of the body. As for the free surface convergence test, the models solved are MS for the free surface domains and NSW in the central one, relative to the fixed structure. The speed of convergence is sub-optimal as we can see from the plot 5(a), where we evaluate the error for the depth and the plot 5(b) for the total pressure. This can be due to the discontinuity in depth and nonlinear term which can not be solved exactly and results in oscillation around the coupling nodes. From the rate of convergence in Π it looks like $m = p$ for every polynomial order tested, losing an order for the odd p in comparison to the continuous model.

We remark here the efficiency of the spectral method: considering a simulation of one period $T = 1.95s$, we fix the time-stepping at $N_t = 5000$ steps and we test different meshes. The efficiency of the

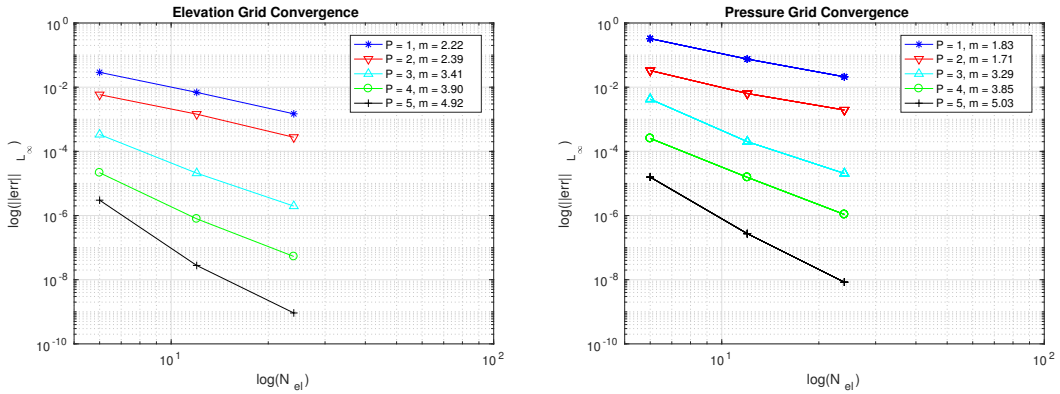

(a) (b)

Figure 5: Convergence trend in a MS-NSW-MS model, with number of elements $N_{el} = [6, 12, 24]$ and polynomial orders $p = [1, 2, 3, 4, 5]$, in figure (a) for the depth variables and in figure (b) for the total pressure variable.

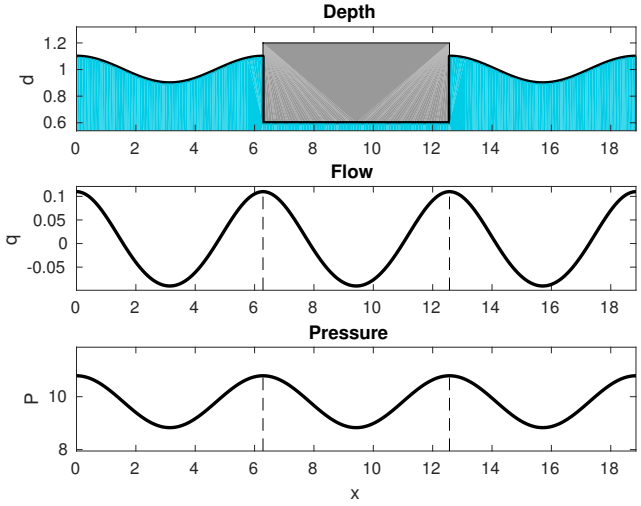

Figure 6: Solution of the manufactured problem for $p = 5$, with number of elements $N = 12$, final time $T = 2s$.

model has been checked for the medium size mesh, with $N = 12$ for each domain. The error drops of of five order between $p = 1$ versus $p = 5$ while the computational time remains comparable ($c_t|_{p=1} = 12.2s$, $c_t|_{p=5} = 48.1s$). On the other hand, if we want to reach a similar precision with linear elements, we need a much finer grid with 1500 DOF per domain against the 60 DOF of the high polynomial order and the computational time grows of 5 orders of magnitude.

4.4 Fixed Pontoon

There are no experimental data on a weakly nonlinear solitary wave propagating past a rectangular box, but this case has been often object of studies in literature as in [30] and [39]. In particular, we are going to concentrate reproducing the VOF-RANS results in [30] and FNPF results [16]. We consider a pontoon of length $L = 5m$ and draft $T_0 = 0.4m$ in a flume of constant still water depth $h_0 = 1.0m$. The two wave gauges are located at $G_1 = -31.5m$ and $G_2 = 26.5m$ assuming the centre of the box located at $x_c = 0m$ as shown in figure 7. The incoming solitary wave is defined by the equation from [4] and has a non-dimensional amplitude $\frac{A}{h_0} = 0.1$. The simulation is done with a mesh of $N_w = 25$ elements on the free surface domain and $N_b = 5$ elements for the body to have a better resolution, the total length of the flume is $185m$ of which $90m$ before the body and $90m$ after, with a polynomial order $p = 3$.

Since the solitary wave is dispersive we can not use the NSW equations as it will not be able to

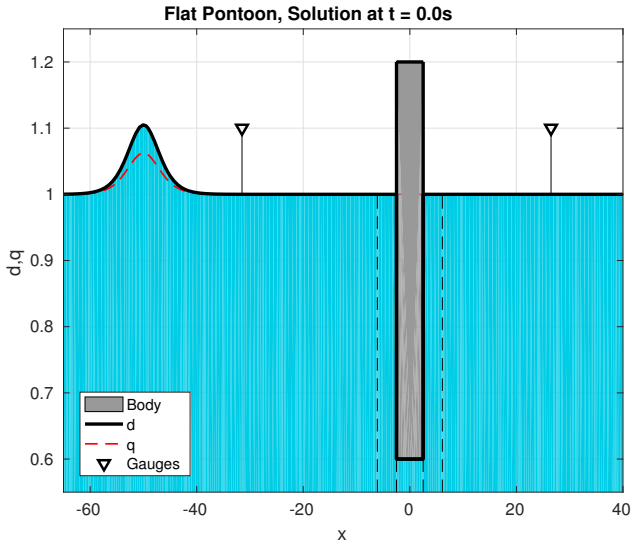

Figure 7: Set of the fixed pontoon problem.

solve it correctly, subsequently the MS model must be used in the outer domain. Anyway, because of proposition 1, we solve the NSW equations in the inner domain. Since the coupling between MS and NSW has been proven effective, especially for free surface flow, we set a small free surface layer around the pontoon where NSW is solved. This layer length must be calibrated and for the purpose of the fixed pontoon we kept it as small as possible to avoid the loss of the dispersive characteristic of the reflected and transmitted waves. Figures 7 and 8 show the solution at different time. The problem is solved correctly, with the wave transmitting and reflecting smoothly against the structure. Few small oscillations are registered on the profile of the internal pressure but they do not seem to affect the solution and the final stability of the method. The comparison between the elevation registered by the gauges in the VOF-RANS simulation and the Madsen and Sørensen is presented in figure 9(a). The wave generated is not perfectly coincident with the wave of the original study, due to the fact that we do not have any information but the wave elevation. This results shows little discrepancies between our solution and the VOF-RANS one, in particular the elevation of the transmitted wave is over-predicted and the first peak of the trail of the reflected wave is under-predicted. However, those differences seem to be of minor importance as the results of two methods are consistent and the simpler Boussinesq model can still capture the salient characteristics of the transmitted and reflected waves. The figure 9(b) shows the total water mass during the simulation, the drops from time $t = 0s$ to $t \approx 20s$ and at the final time, represent the absorption of a trail from the incident soliton wave and of the resulting waves in the sponge zone. Anyway we can see that, once the trail is absorbed (around $t \approx 20s$) and before time $t \approx 37s$ when the waves are absorbed, the mass is conserved.

This model can be easily modified to solve the case of a fixed pontoon with different bottom shapes and see how this affect the transmitted and reflected wave. In particular we tested a triangular bottom in figure 10(a), a round parabolic bottom, figure 10(b) and a flat bottom with a deeper submerged area 10(c). The non-squared pontoons are designed to have a submerged volume equal to the one of the first test in figure 7. The mesh is the same as for the previous pontoon test.

We notice from the solutions of the different pontoons in figures 8(c), 11(c), 12(c) and 13(c) for time $14.44s$ and 8(f), 11(f), 12(f) and 13(f) for time $16.44s$, is how the shape affects the profile of the inner pressure. However the transmitted and reflected waves are very similar to the original test, as we can see from the gauges plot in figure 14(a). This is because for the fixed body setting is more important the volume (area in 2D) of water occupied more than the shape or the maximum depth. This is confirmed by the last test in figure 10(c), where we have a flat bottom pontoon that reaches the same maximum depth of the triangular one thus occupying a much larger area. From the gauges in figure 14(a) we see a substantial difference as the reflected wave is higher and the transmitted smaller. The force applied vertically by the wave on the bottom of the body in figure 14(b) is very similar in all the tests with the biggest difference shown once the peak of the wave has passed the body.

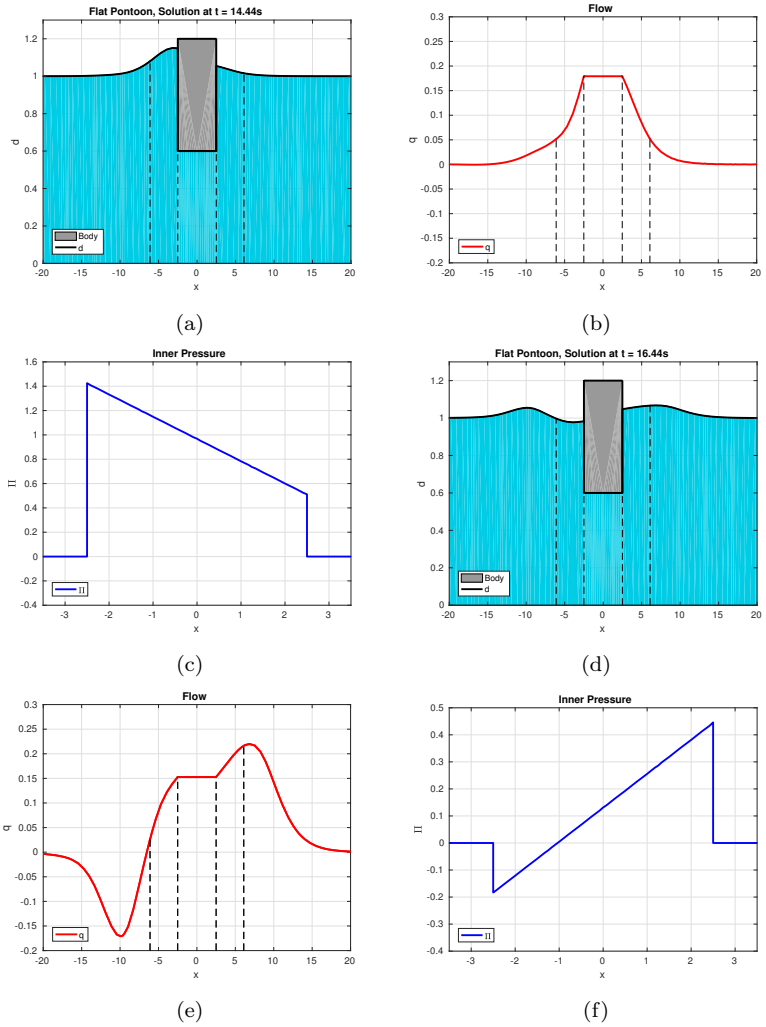

Figure 8: Snapshot of the pontoon interacting with the incoming soliton, at maximum wave elevation (time $14.44s$) (a) wave elevation, (b) wave flow and (c) Inner pressure; at minimum wave elevation ($16.44s$) (d) wave elevation, (e) wave flow and (f) Inner pressure.

4.5 Forced motion test

The test includes forced oscillation of a box with a round bottom, shown in figure 15(a). The body is placed with its centre at $x = 0$ and the water flume extends for $200m$ before and after it. This is composed by a rectangular box of height $H = 2R\sin(\pi/3) - R$ and width $2R$ and, at the bottom, a circular segment of a disk of radius $2R$ which centre is placed above the top side of the solid, over the vertical line passing through the middle point C of the side. The density of the object is half the density of water, $\rho_b = 0.5\rho_w$. We can easily evaluate the mass of the object $m = \rho_b \mathcal{V}$ where $\mathcal{V}$ is the volume

$$\mathcal{V} = R^2 \left(\sqrt{3} - 2 + \frac{2\pi}{3} \right). \tag{75}$$

In both tests, we use $R = 10m$. We define the fluid domain with a still-water depth $h_0 = 15m$ and density of water $\rho_w = 1000kgm^{-3}$. The structure moves in forced motion starting from initial position $z_{C,eq} = 4.57m$ and an oscillation of $2m$ over $10s$ time. This height corresponds to the equilibrium position in case of the free floating object and can be calculated as

$$z_{C,eq} = \frac{R}{2} \left(1 - \frac{\rho_b}{\rho_w} \right) \left(\sqrt{3} - 2 + \frac{2\pi}{3} \right). \tag{76}$$

The setting for the decay and forced test is the same: polynomial order $p = 3$, $N_w = 25$ external nodes and $N_b = 5$ internal ones.

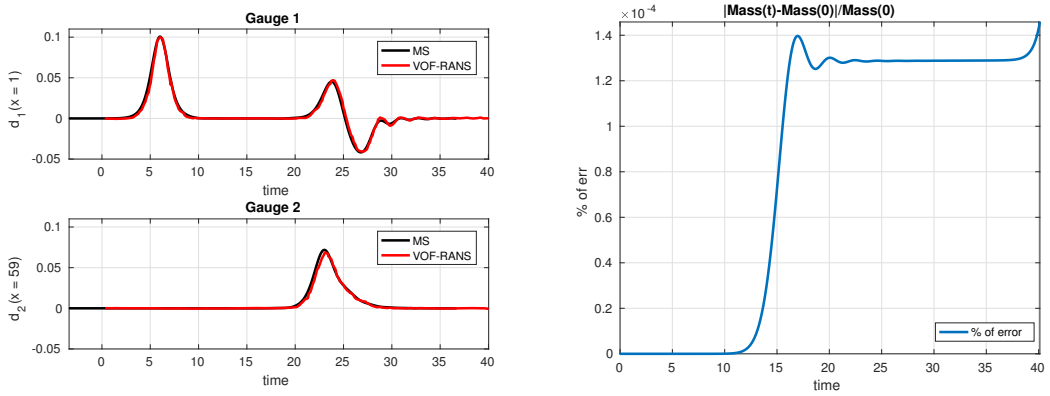

(a) (b)

Figure 9: (a) Elevation at the two gauges; (b), error in the total water mass during the simulation.

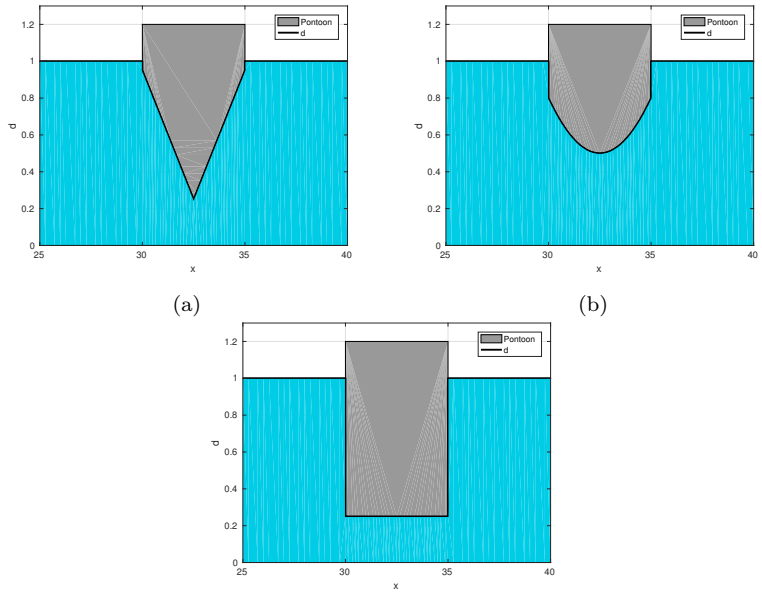

(a) (b)

(c)

Figure 10: Shapes tested, (a), (b) and (c) initial set.

In the hydrostatic case, we have an analytic solution for the water elevation at the contact points x_+ and x_-, where water and body interact, from [28]. The evolution of the water level at $x_\pm$ is described by

$$d_e(t, x_\pm) = \left(\tau_0 \left(\frac{x_+ - x_-}{4\sqrt{g}} v_g \right) \right)^2, \tag{77}$$

$v_G = d_t$ is the given velocity of the center of gravity of the object. The parameter τ_0 is obtained from

$$\tau_0(r) = \frac{1}{3} \left(\sqrt{h_0} + C(r) + \frac{h_0}{C(r)} \right), \tag{78}$$

with $C(r)$ given by

$$C(r) = \frac{3}{2} \left(-4r + r_0 + \sqrt{r(r - r0)} \right)^{\frac{1}{3}}, \tag{79}$$

and $r_0 = \frac{4}{27} h_0^{\frac{3}{2}}$.

From the figure 16, presents a convergence study. We get a lower rate of convergence for all the mesh tested, compared to the results of sections 4.2 and 4.3. This is probably due to the fact that the initialisation of the first two steps of BDF3 method are evaluated with Euler and the error is then propagated to the rest of the simulation.

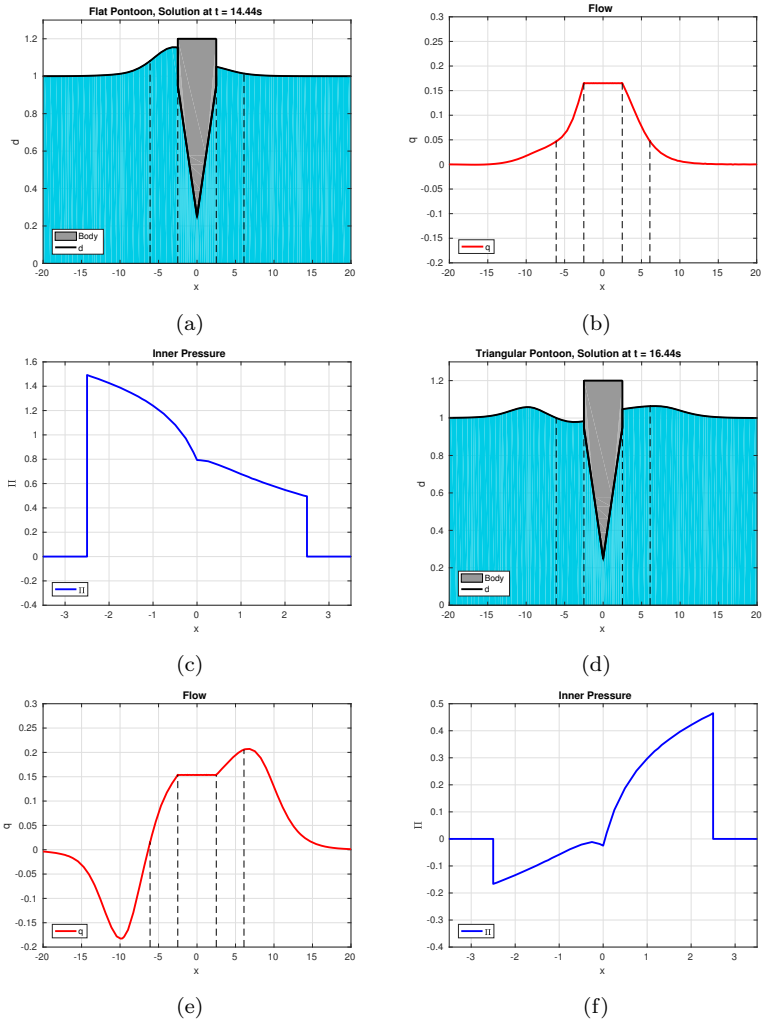

Figure 11: Snapshot of the triangular pontoon interacting with the incoming soliton, at maximum wave elevation (time 14.44s) (a) wave elevation, (b) wave flow and (c) Inner pressure; at minimum wave elevation (16.44s) (d) wave elevation, (e) wave flow and (f) Inner pressure.

As proof of concept he forced test is done with the outer domain solved with the MS model. We don't have any exact solution to compare it to but we can see from the figure 17(e) that the MS solution is not far from the NSW and even if it presents few oscillations in the position of the contact point in the upward movement, the transmitted wave seems smooth and well resolved. It's interesting to notice also the difference in the wave front in the two cases: while we see a sharp wave front for the NSW model in figures 15(a), 15(b), 15(c) and 15(d), the MS model smooths the outgoing wave in figures 17(a), 17(b), 17(c) and 17(d).

4.6 Decay test

For the decay test, we consider the same structure 18(a) freely floating in the vertical direction, from an initial position $z_{C,0}$ different from the equilibrium one $z_{C,eq}$. In our simulation the object starts with the center of gravity below the water line $z_{C,0} = z_{C,eq} - 2m$ and it returns to the equilibrium position. We can validate the model solving the semi-analytical solution for the movement of the body's center of gravity, given by the differential equation in [28]

$$\begin{cases} (m_b + m_{add})\ddot{\delta_G} = -c\delta_G - \nu(\dot{\delta_G}) + \beta(\delta_G)(\dot{\delta_G})^2 \\ (\delta_G, \dot{\delta_G})(t=0) = (\delta_G^0, 0), \end{cases} \tag{80}$$

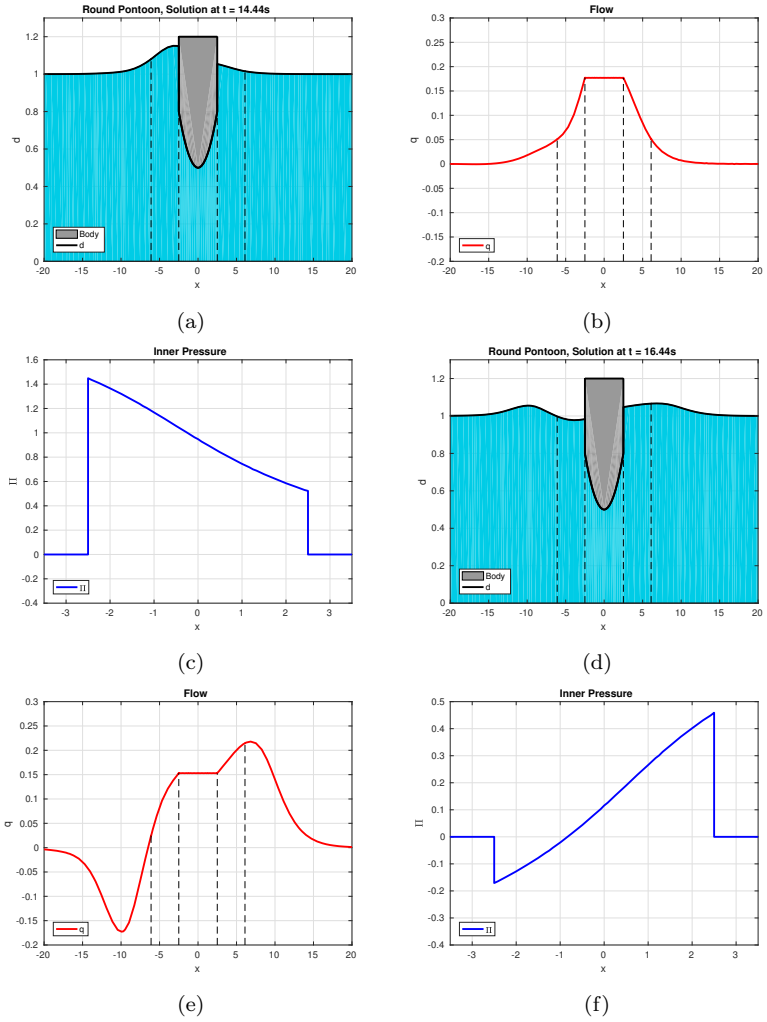

Figure 12: Snapshot of the round pontoon interacting with the incoming soliton, at maximum wave elevation (time 14.44s) (a) wave elevation, (b) wave flow and (c) Inner pressure; at minimum wave elevation (16.44s) (d) wave elevation, (e) wave flow and (f) Inner pressure.

the parameters $\nu(\dot{\delta_G})$ and $\beta(\delta_G)$ are defined as

$$\begin{aligned}\nu(\dot{\delta_G}) &= \rho_w g(x_+ - x_-)\left[h_0 - \left(\tau_0\left(\frac{x_+ - x_-}{4\sqrt{g}}\dot{\delta_G}\right)\right)^2\right],\\ \beta(\delta_G) &= \rho_w \int_{x_-}^{x_+} \frac{x - x_0}{h_w}\partial_x\left(\frac{(x-x_0)^2}{h_w}\right)dx,\end{aligned} \tag{81}$$

with $h_w(t) = d_{eq} + \delta_G(t)$ the position of the wetted surface and describes the geometry of the bottom of the body, and $\zeta_{e,\pm} = \zeta_e(t, x_\pm) = d_e(t, x_\pm) - h_0$. The added mass term m_{add} and the stiffness coefficient c

$$\begin{aligned}m_{add} &= \rho_w Var(x)\alpha \quad \alpha = \int_{x_-}^{x_+}\frac{1}{h_w}dx,\\ c &= \rho_w g(x_+ - x_-).\end{aligned} \tag{82}$$

We define a variance operator as

$$\begin{aligned}Var(f) &= \langle f^2\rangle - \langle f\rangle^2,\\ \langle f\rangle &= \frac{1}{\int_{x_-}^{x_+}\frac{1}{h_w}}\int_{x_-}^{x_+}\frac{f}{h_w}dx.\end{aligned} \tag{83}$$

The ODE (80) is solve with a BDF3 time integration scheme, such that the integration is consistent with one of the numerical problem. In figure 18(e) we see the tracking of the center of gravity and the two

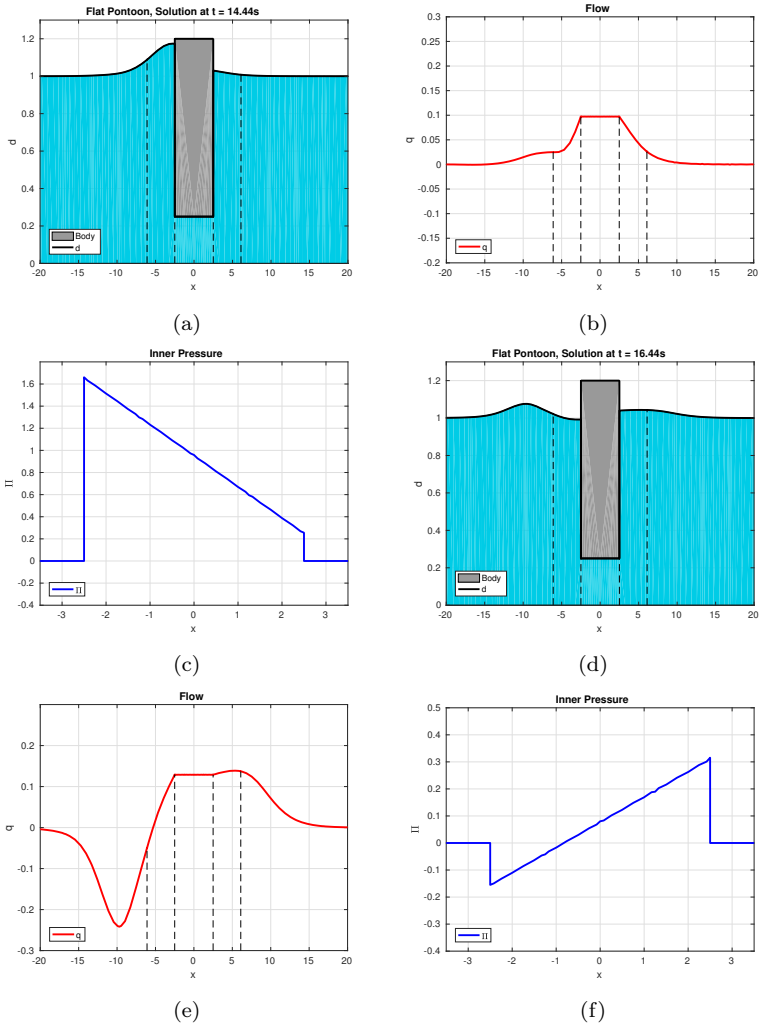

Figure 13: Snapshot of the flat deep pontoon interacting with the incoming soliton, at maximum wave elevation (time 14.44s) (a) wave elevation, (b) wave flow and (c) Inner pressure; at minimum wave elevation (16.44s) (d) wave elevation, (e) wave flow and (f) Inner pressure.

methods give comparable solution.

We can evaluate the same decay test with the MS model for the outer domain. The evolution of the solution, shown in figures 19(a), 19(b), 19(c) and 19(d) is significantly different from the NSW solution, in figure 18(a) to 18(d)

5 Heaving Body

We now test a heaving box interacting with a stream function wave evaluated by a stream function as in [18]. The body is a rectangular box of length $l = 6m$ and heigth $= 10m$, with a displacement of $30m^2$. Because of the characteristics of the waves generated, the outer domain must be solved with the MS equations. As in section 4.4 we define a small free surface layer around the body where we solve the NSW equations, coupled with the inner NSW model. The layer here is calibrated to be long enough such that we avoid the propagation of dispersive terms under the body, where they are equal to zero and short enough to permit the propagation of the wave with a minimal distortion. In practice, we have seen that $L_{NSW} = \frac{\lambda}{5}$, gives acceptable results.

We tested three set of waves of increasing steepness $\sigma = \frac{A}{\lambda}$, where A is the wave amplitude and λ the wave length. These are listed in the table 1. The main results in figure 21 are presented in terms of the Response Amplitude Operator (RAO), which is evaluated as

$$RAO = \frac{Max(\eta_i) - min(\eta_i)}{2A}, \tag{84}$$

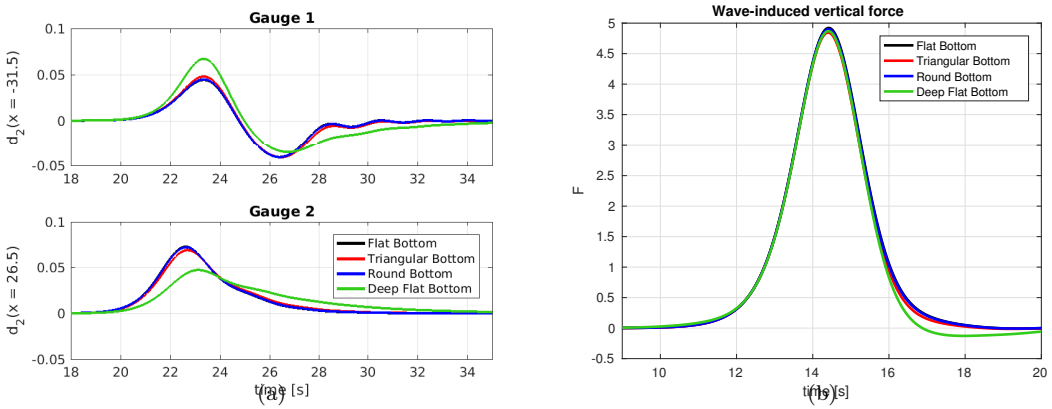

Figure 14: (a) Elevation at the two gauges and (b) Force induced by the action of the wave under the body.

Period $T[s]$	Amplitude $A[m]$	Steepness $\sigma[-]$
6.00	2.75×10^{-3}	10^{-4}
7.00	3.6×10^{-3}	10^{-4}
8.01	4.45×10^{-3}	10^{-4}
9.99	6.05×10^{-3}	10^{-4}
5.99	0.69	0.025
6.99	0.9	0.0249
8.01	1.12	0.025
10.01	1.53	0.025
5.97	1.38	0.0495
6.95	1.8	0.0494
7.92	2.23	0.0497

Table 1: Period, amplitude and steepness of the wave tested

where η_i is the elevation of the body. We notice that, for linear waves in figure 21(a), we can retrace the behaviour of the linear model, with the characteristic peak at the resonance frequency. For wave with a low steepness of $\sigma = 0.025$, we have a RAO close to the CFD model where the peak at $T = 6s$ is about half the result for the linear model. For higher value of steepness the RAO, in figure 21(c), of the Boussinesq model has a value halfway between the linear and the RANS result. Note that for the fastest and shortest waves ($T < 6s$) we don't have any result as we are outside the application window of the MS-Boussinesq model, suggesting that a Boussinesq model with improved properties could be used instead.

6 Multiple Bodies

With our framework, we can use the domain decomposition in a setup to simulate multiple bodies. In this section we consider a two bodies configuration, as in figure 22. Each body can be alternatively fixed or a heaving. Both bodies have length $l = 6m$ and heigth $h_b = 10m$. The dimension of the free surface domains is defined by the length of the wave tested, such that we can accomodate the generation and the absorption layer. The left free surface is 5λ long, the central one is 2λ and the last, after the second body is 4λ. The NSW layer around the bodies is a single element of lentgh equal to a fifth of a wave length. The polinomial order is $P = 3$.

The figure 23 shows the response of the moving bodies of the simulations to four set of waves of period $T = [6, 7, 8, 10]s$ and steepness $\sigma = [0.0001, 0.025]$. We can see from the figure 23, that the interaction of the transmitted and reflected waves for the two bodies affects the RAO. We can see that, a part from the short linear wave where the single body (the dashed line in the plots) is at resonance frequency, the first body (blue stars and squares $*$, $\square$) benefits by the reflected waves on the second one (red Xs and triangles $\times$, $\triangleleft$), especially when the latter is another heaving body. It's interesting to notice that the variations of the RAO of the two bodies present similar trends to the single body RAO. This is probably

do to the fact that the space between the to bodies is not fixed through the different simulations but it is always proportional to the wave length. We expect that the RAO can vary with less predictable trends in case the distance is fixed. This can be seen for example in figure 24, where the distance between the two bodies is fixed at 20 metres. In this case the reflected wave has a dampening impact on the movement of the first body, resulting in it having a smaller movement than the second one in most cases. This test shows also the importance, in the future, to be able to optimize the placement of several bodies in such a way that the constructive behaviours are enhanced and the destructive ones minimized.

7 Conclusion

We have presented three nonlinear numerical models for a heaving point absorber, in particular the nonlinear shallow water equations and the Madsen and Sørensen equations. These models are based on depth-integrated Boussinesq-type equations, a computationally efficient method for sea state in near-shore waters. The unified approach of Jiang [25] inspired the model, the recent work of Lannes [28] the added mass approach to the definition of the acceleration and finally the discontinuous coupling by Eskilsson and Sherwin [21] a weak coupling formulation between the different domains.

We tested the coupling for the free surface case, with a convergence study where we demonstrated the spectral convergence of the method. Finally we have validated our model against previous results. The simulation for the fixed pontoon shows a similar outcomes for our Boussinesq model and the CFD solution by Lin [30]. For the moving structure we can reproduce the results of Lannes [28] and we have agreement with the exact solution. The results shows that we can simulate different shapes of body. The results for the heaving floating body show agreement with assessed result for linear and small steepness wave and a clear improvement in case of medium steepness compered to the linear model. The next step is to include some form of optimal control such that we can optimize the power outpout of the device. In addition, we aim to expand the framework to two spatial dimensions in the free surface plane and include more degree of freedom for the body. However, there are few problems related in primis to the instabilities that arise in the MS-NSW coupling or in evaluation the inner pressure. A smoothing and stabilizing method must be implemented for the evaluation of the pressure, such that the solution can be evaluated more efficiently.

In spite of these challenges ahead we believe the present work indicates that a medium-fidelity Boussinesq based model can bring benefits in terms of efficiency without compromising on the accuracy of the results.

In ongoing work, we will consider the extension to two horizontal space dimensions and add another degree of freedom to the model, permitting the body to sway or surge with the arbitrary Lagrangian Eulerian technique.

Acknowledgement

This work was performed within the Ocean ERANET project MIDWEST, funded by the French agency ADEME, Swedish Energy Agency SWEA and Portuguese agency FCT. We warmly thank Dr. D. Lannes for many useful and interesting discussions and suggestions.

A Dimensional Analysis

The dispersive and nonlinear characteristic of shallow water waves are described in the Boussinesq approximation by two parameters: the dispersive parameter

$$\mu = \frac{2\pi h_0}{\lambda} = k h_0 \tag{85}$$

defined as the ratio between the still water depth h_0 (or average depth in case of a non constant bathymetry) and the wave length λ; and the nonlinearity parameter

$$\varepsilon = \frac{A_o}{h_0} \tag{86}$$

defined as the ratio between the wave elevation A_0 and the depth. The Boussinesq theory considers $\mu^4 \ll 1$ and $\mu^2 \approx \varepsilon$. Based on this two parameters, we can perform a nondimensional analysis of the

variables

$$
\begin{aligned}
&\tilde{t} = \frac{2\pi\sqrt{gh_0}}{\lambda} t = \mu \frac{\sqrt{gh_0}}{h_0} t, \\
&(\tilde{x}, \tilde{y}) = \frac{2\pi}{\lambda}(x, y) = \frac{\mu}{h_0}(x, y), \\
&\tilde{z} = \frac{z}{h_0}, \\
&\tilde{h}(\tilde{x}, \tilde{y}) = \frac{h(x, y)}{h_0} = 1, \\
&\tilde{\eta}(\tilde{x}, \tilde{y}, \tilde{t}) = \frac{\eta(x, y, t)}{A_0} = \frac{\eta(x, y, t)}{\varepsilon h_0}, \\
&\tilde{d}(\tilde{x}, \tilde{y}, \tilde{t}) = \tilde{\eta}(\tilde{x}, \tilde{y}, \tilde{t}) + \tilde{h} = \frac{d(x, y, t)}{\varepsilon h_0}, \\
&\tilde{\boldsymbol{u}} = \frac{1}{\varepsilon\sqrt{gh_0}} \boldsymbol{u}, \\
&\tilde{\boldsymbol{q}} = \tilde{d}\tilde{\boldsymbol{u}}, \\
&\tilde{w} = \frac{\mu}{\varepsilon\sqrt{gh_0}} w, \\
&\tilde{P} = \frac{1}{\varepsilon\rho_w g h_0} P,
\end{aligned}
$$

where η is the istantaneous wave elevation and w the vertical velocity component. The non dimensional MS problem reads

$$
\begin{aligned}
&\rho_w \tilde{P}_t + \nabla \cdot \tilde{\boldsymbol{q}} = \mathcal{O}(\mu^2, \epsilon), \\
&\tilde{\boldsymbol{q}}_t - \mu^2 B \nabla(\nabla \cdot \tilde{\boldsymbol{q}}_t) + \varepsilon \nabla \cdot (\tilde{u} \otimes \tilde{q}) + \varepsilon \rho_w \tilde{d} \nabla \tilde{P} + \alpha_{MS} \varepsilon \mu^2 \rho_w g \nabla(\Delta \tilde{P}) = \mathcal{O}(\mu^2, \varepsilon).
\end{aligned}
\tag{87}
$$

References

[1] Abbott, M.B., Petersen H.M. and Skovgaard O. Computations of short waves in shallow water. Coastal Engineering (1978): 414-433.

[2] Abbott, M.B., Petersen H.M. and Skovgaard O. On the numerical modelling of short waves in shallow water. Journal of Hydraulic Research 16.3 (1978): 173-204.

[3] Agamloh, E. B., Wallace, A. K. and von Jouanne, A. Application of fluid–structure interaction simulation of an ocean wave energy extraction device. Renewable Energy 33.4 (2008): 748-757.

[4] Bonneton, P., Chazel F., Lannes D., Marche F. and Tissier M. A splitting approach for the fully nonlinear and weakly dispersive Green–Naghdi model. Journal of Computational Physics 230.4 (2011): 1479-1498.

[5] Brocchini M. A reasoned overview on Boussinesq-type models: the interplay between physics, mathematics and numerics. Proc. R. Soc. A. 469.2160 (2013): 20130496.

[6] Castro M.J., LeFloch P.G., Muñoz-Ruiz M.L., Parés C.. Why many theories of shock waves are necessary: Convergence error in formally path-consistent schemes. Journal of Computational Physics 227.17 (2008): 8107-29.

[7] Chen, X.N. and Sharma, S. A slender ship moving at near-critical speed in a shallow channel. Journal of Fluid Mechanics 291 (1995): 263-285.

[8] Cockburn, B. and Shu, C.-W. The local discontinuous Galerkin method for time-dependent convection-diffusion systems. SIAM Journal on Numerical Analysis, 35.6 (1998): 2440-2463.

[9] Cummins, W. E. The impulse response function and ship motions. No. DTMB-1661. David Taylor Model Basin Washington DC, (1962).

[10] Dumbser M., Castro M., Parés C., Toro E.F. ADER schemes on unstructured meshes for nonconservative hyperbolic systems: Applications to geophysical flows. Computers & Fluids 38.9 (2009): 1731-48.

[11] Dumbser, M. and Facchini, M. A space-time discontinuous Galerkin method for Boussinesq-type equations. Applied Mathematics and Computation 272 (2016): 336-346

[12] Duran, A., Dutykh D. and Mitsotakis D. On the Galilean invariance of some nonlinear dispersive wave equations. Studies in Applied Mathematics 131.4 (2013): 359-388.

[13] Duran, A. and Marche, F. Discontinous-Galerkin discretization of a new class of Green-Nagdhi equations. Communications in Computational Physics 17.3 (2015):572-588.
[14] Engsig-Karup A.P., Eskilsson C., Bigoni D. A stabilised nodal spectral element method for fully nonlinear water waves. Journal of Computational Physics 318 (2016):1-21.
[15] Engsig-Karup, A.P., Hesthavem J.S., Bingham, H. and Madsen. P. Nodal DG-FEM solutions of high-order Boussinesq-type equations. Journal of Engineering Mathematics 56 (2006):351-370.
[16] Engsig-Karup, A.P., Monteserin C. and Eskilsson C. A Stabilised Nodal Spectral Element Method for Fully Nonlinear Water Waves, Part 2: Wave-body interaction. arXiv preprint arXiv:1703.09697 (2017).
[17] Ertekin, R., Webster, W. and Wehausen, J. Waves caused by a moving disturbance in a shallow channel of finite width. Journal of Fluid Mechanics 169 (1986): 275-292.
[18] Eskilsson, C., Palm, J., Engsig-Karup, A.P., Bosi, U. and Ricchiuto, M. Wave Induced Motions of Point-Absorbers: a Hierarchical Investigation of Hydrodynamic Models. 11th European Wave and Tidal Energy Conference (EWTEC). (2015).
[19] Eskilsson, C., Palm J., Kofoed J. P. and Friis-Madsen E. CFD study of the overtopping discharge of the Wave Dragon wave energy converter. Renewable Energies Offshore (2015): 287-294.
[20] Eskilsson, C. and Sherwin S.J. A discontinuous spectral element model for Boussinesq-type equations, Journal of Scientific Computing 17.1 (2002): 143-152.
[21] Eskilsson, C. and Sherwin S.J. Spectral/hp discontinuous Galerkin methods for modelling 2D Boussinesq equations, Journal of Computational Physics 212.2 (2006): 566-589.
[22] Filippini, A.G, Bellec S., Colin M. and Ricchiuto M. On the nonlinear behaviour of Boussinesq type models: Amplitude-velocity vs amplitude-flux forms, Coastal Engineering 99 (2015): 109-123 .
[23] Hesthaven JS, Warburton T. Nodal discontinuous Galerkin methods: algorithms, analysis, and applications. Springer Science & Business Media (2007).
[24] Horn RA, Johnson CR. Matrix analysis. Cambridge university press; (1990).
[25] Jiang, T. Ship waves in shallow water. Fortschritt-Berichte VDI Reihe 12, Verkehrstechnik, Fahrzeugtechnik; (2001).
[26] John, F. On the motion of floating bodies. Part I. Communications on Pure and Applied Mathematics 2 (1949):13-57
[27] Karniadakis, G. and Sherwin S.J. Spectral/hp element methods for computational fluid dynamics, Oxford University Press (2013).
[28] Lannes, D. On the dynamics of floating structures, Annals of PDE 3.1 (2017): 11.
[29] Lannes, D., private communications and notes.
[30] Lin, P. A multiple-layer σ-coordinate model for simulation of wave–structure interaction. Computers & fluids 35.2 (2006): 147-167.
[31] Madsen, P.A. and Schäffer H.A. A review of Boussinesq-type equations for surface gravity waves. Advances in Coastal and Ocean Engineering (1999): 1-94.
[32] Madsen, P.A. and Sørensen O.R. A new form of the Boussinesq equations with improved linear dispersion characteristics. Part 2. A slowly-varying bathymetry. Coastal Engineering 18.3-4 (1992): 183-204.
[33] Martinelli, L. and Ruol P. 2D Model of floating breakwater dynamics under linear and nonlinear waves. COMSOL users conference. (2006).
[34] Muñoz-Ruiz, M.L. and Parés, C. On the convergence and well-balanced property of path-conservative numerical schemes for systems of balance laws. Journal of Scientific Computing 48.1-3 (2011): 274-295.
[35] Nørgaard, J. and Andersen, T. Investigation of wave transmission from a floating Wave Dragon wave energy converter. In Proceedings of the 22nd International Offhore and Polar Engineering Conference, Rhodes, Greece (2012)
[36] Palm, J., Eskilsson, C., Paredes, G. M. and Bergdahl, L. CFD simulation of a moored floating wave energy converter. In Proceedings of the 10th European Wave and Tidal Energy Conference, Aalborg, Denmark (Vol. 25). (2013)
[37] Peregrine, D.H. Long waves on a beach. Journal of fluid mechanics 27.4 (1967): 815-827.
[38] Ricchiuto, M. and Filippini, A. G. Upwind residual discretization of enhanced Boussinesq equations for wave propagation over complex bathymetries. Journal of Computational Physics 271 (2014): 306-341.
[39] Rijnsdorp, D.P. and Zijlema M. Simulating waves and their interactions with a restrained ship using a non-hydrostatic wave-flow model. Coastal Engineering 114 (2016): 119-136.
[40] Samii, A. and Dawson, C. An explicit hybridized discontinuous Galerkin method for Serre-Green-

Nagdhi wave model. Computer Methods in Applied Mechanics and Engineering 330 (2018): 447-470.
[41] Toro, E.F. Riemann solvers and numerical methods for fluid dynamics: a practical introduction. Springer Science & Business Media. (2013).
[42] Yan, J. and Shu, C.-W. Local discontinuous Galerkin methods for partial differential equations with higher order derivatives. Journal of Scientific Computing, 17.1-4 (2002): 27-47.
[43] Yu, Y.H. and Ye, L. Reynolds-Averaged Navier–Stokes simulation of the heave performance of a two-body floating-point absorber wave energy system. Computers & Fluids 73 (2013): 104-114.

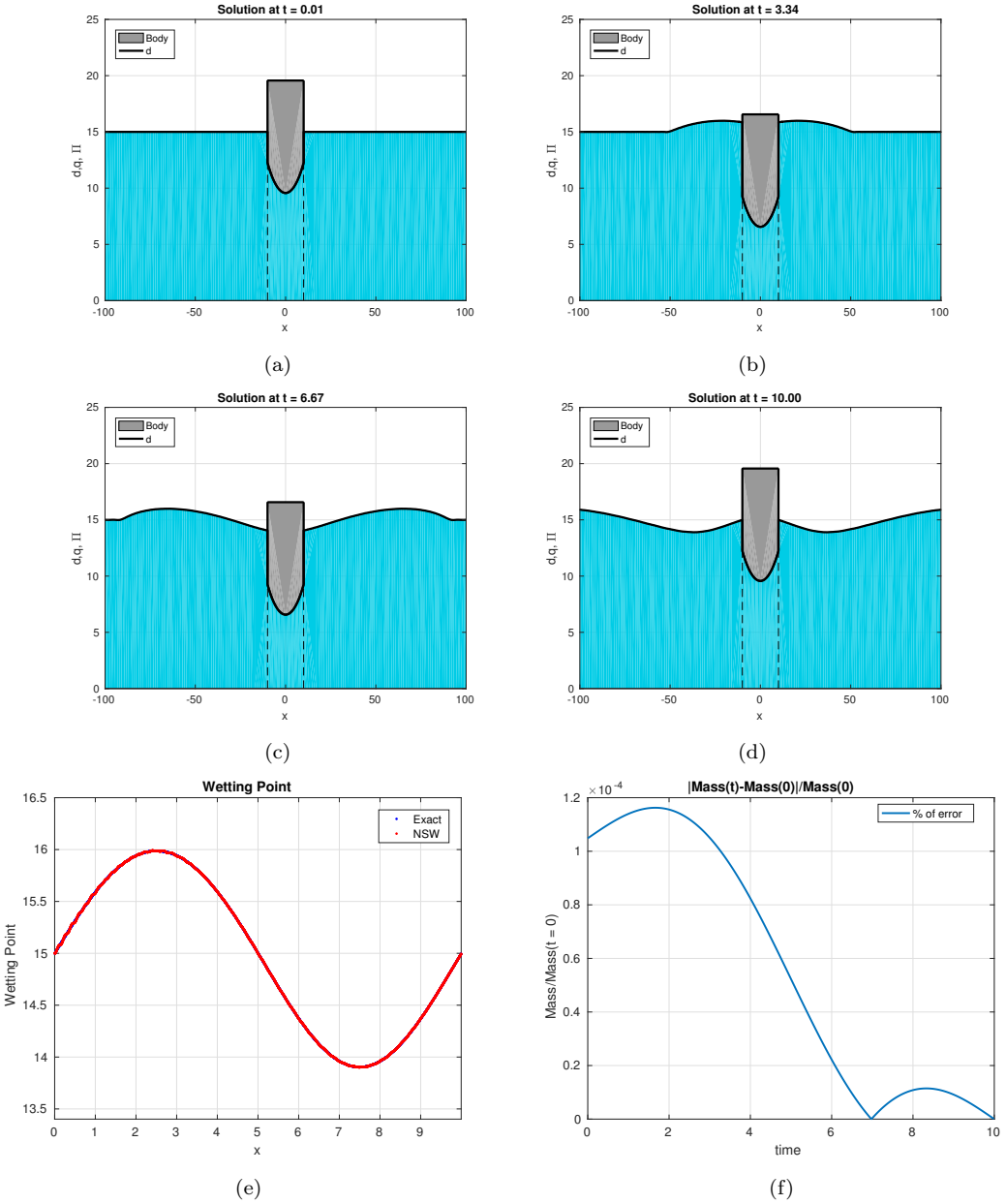

Figure 15: Snapshot of the forced motion test case: (a) initial state, (b) solution at $t = 3.33s$, (c) solution at $t = 6.66s$, 15(d) solution et $t = 10s$. Figure (e) shows the evolution of the contact point and the exact solution from eq. (77). Figure (f) shows the amount of error on the total mass during the simulation.

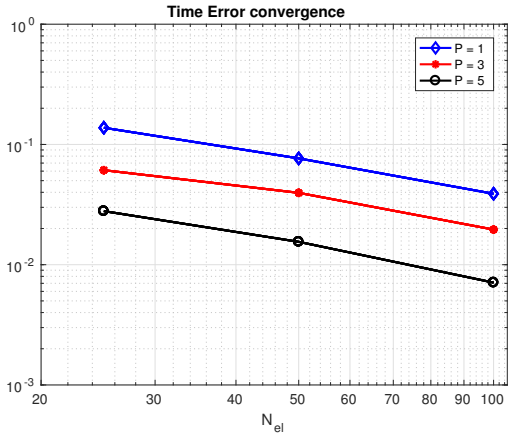

Figure 16: Convergence in time for the forced motion test

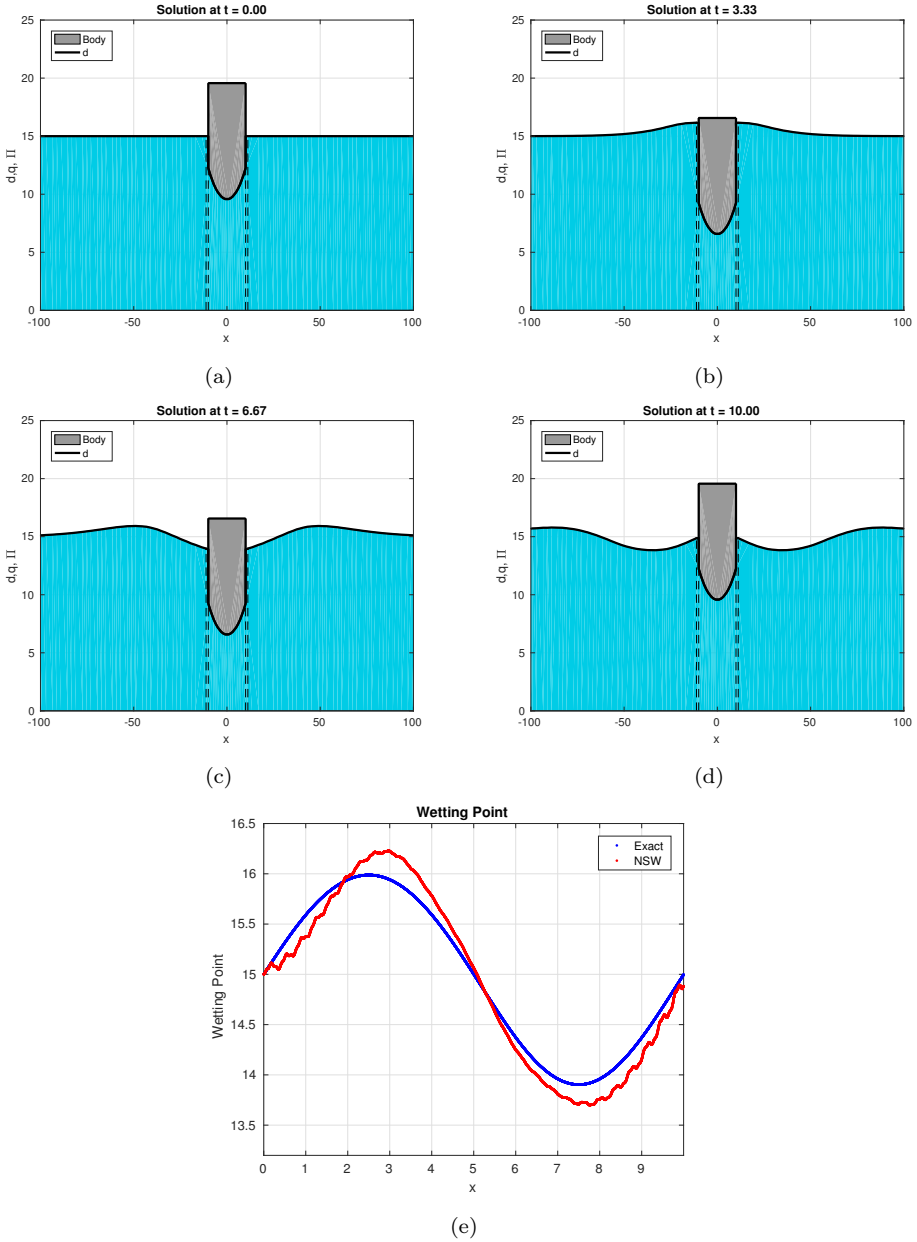

Figure 17: Snapshot of the forced motion test case: (a) initial state, (b) solution at $t = 3.33s$, (c) solution at $t = 6.66s$, 15(d) solution at $t = 10s$. Figure (e) shows the evolution of the contact point and the exact solution from eq. (77).

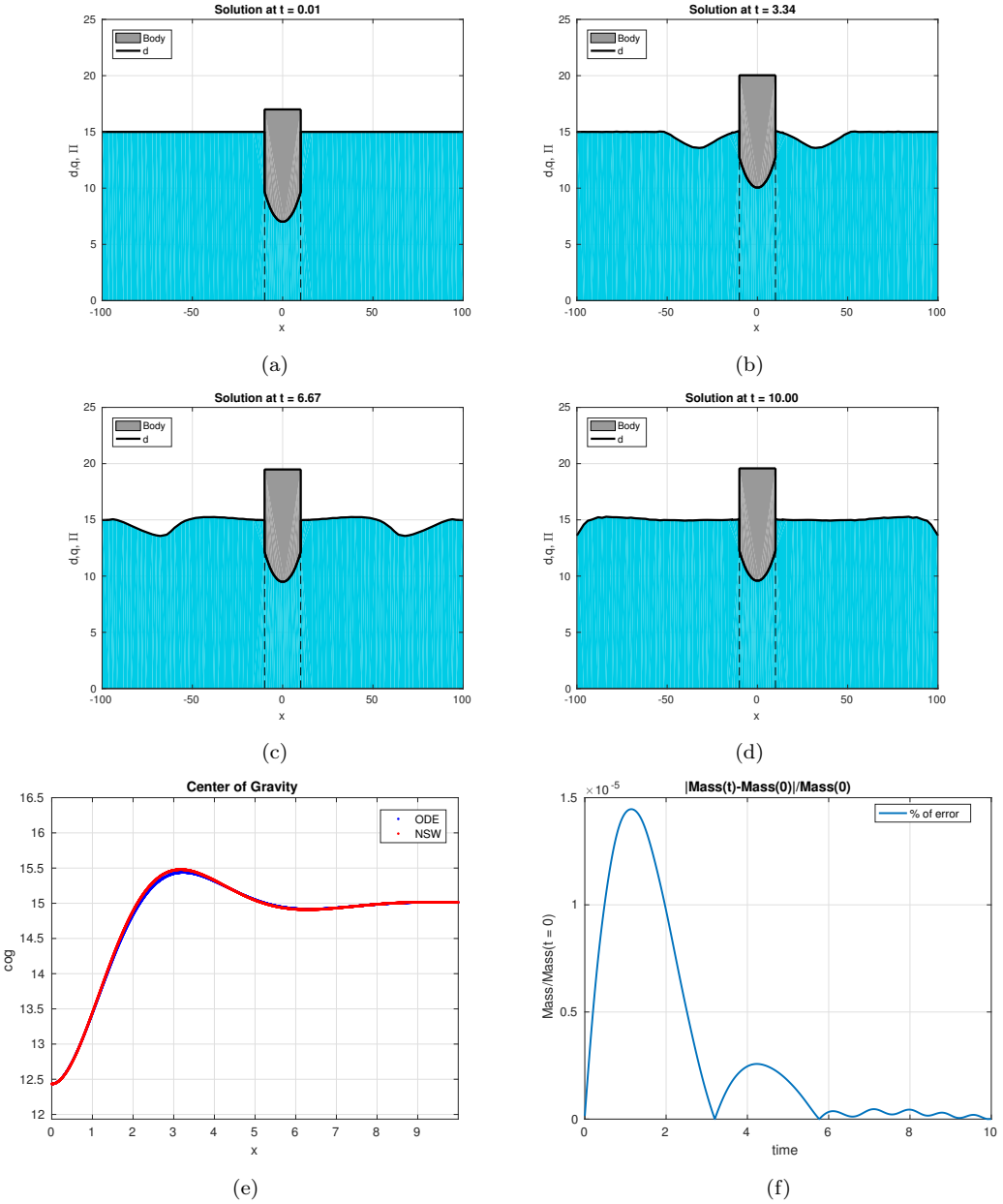

Figure 18: Snapshot of the decay test case: (a) initial state, (b) solution at $t = 3.33s$, 18(c) solution at $t = 6.66s$, (d) solution at $t = 10s$. Figure (e) shows the evolution of the center of gravity and the exact solution and figure (f) the conserved mass of water during the simulation.

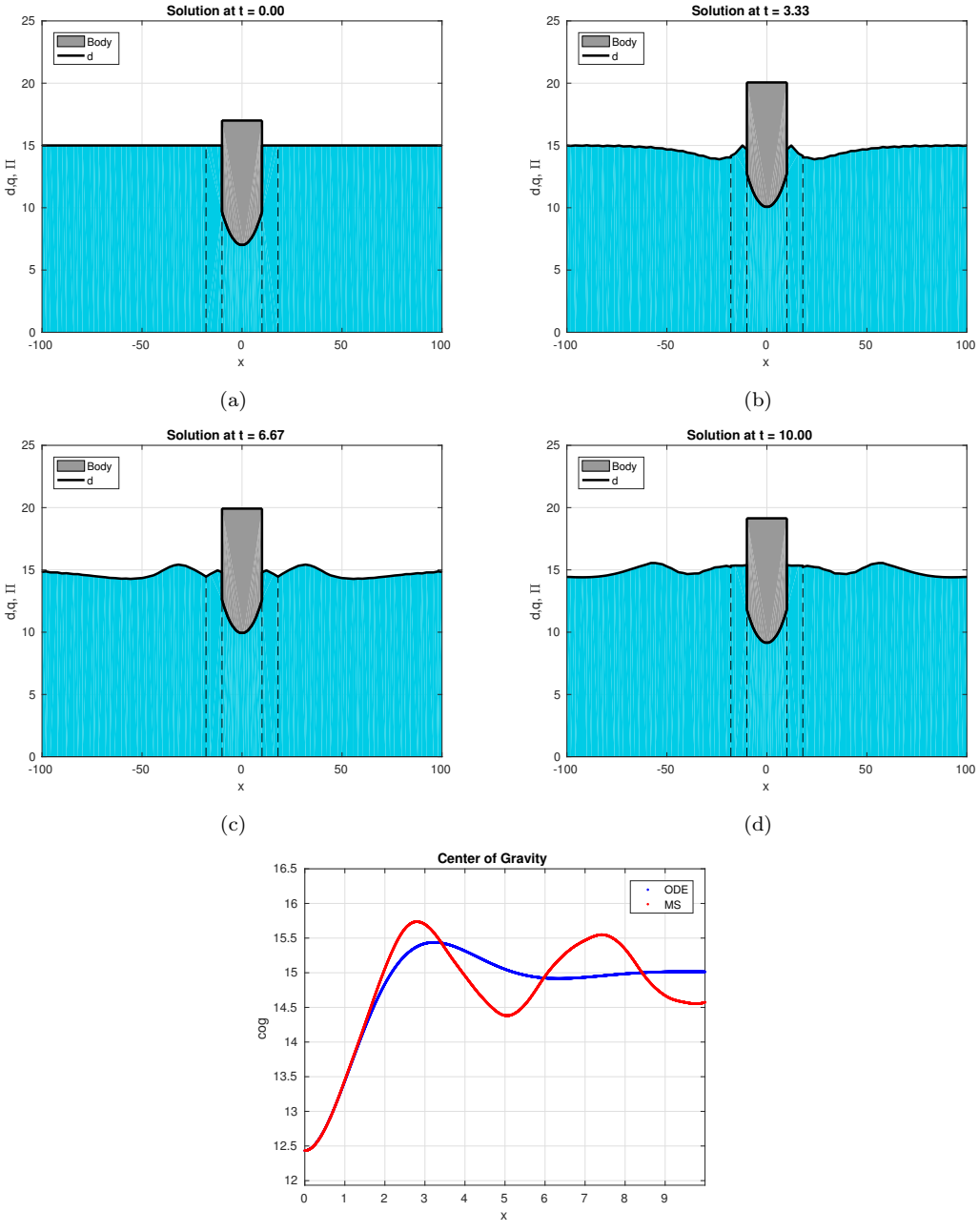

Figure 19: Snapshot of the decay test case with Madsen and Sørensen model: figures (a), (b), (c) and (d) shows the evolution of the solution between $t = [0, 10]s$. Figure (e) shows the evolution of the center of gravity and the exact solution.

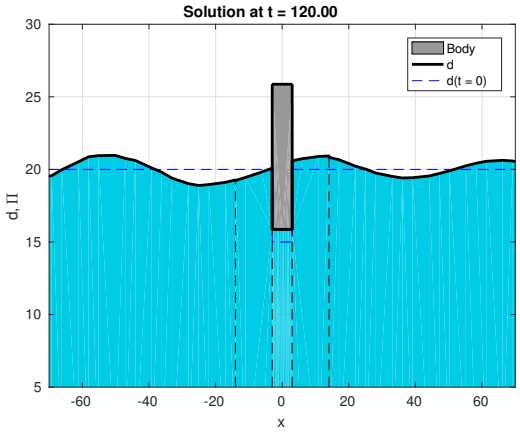

Figure 20: Particular of the heaving body after $120s$, for a stream wave of period $T = 6s$ and steepness $\sigma = 0.025$.

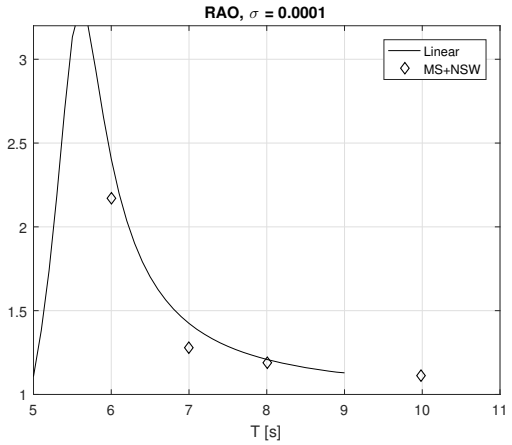

(a) RAO plot for a linear wave of steepness $\sigma = 0.0001$ for a heaving body

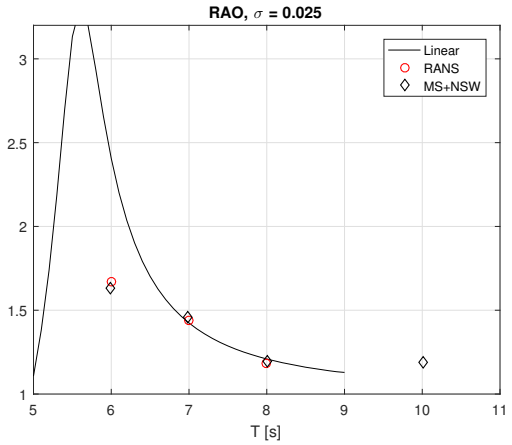

(b) RAO plot for a heaving body

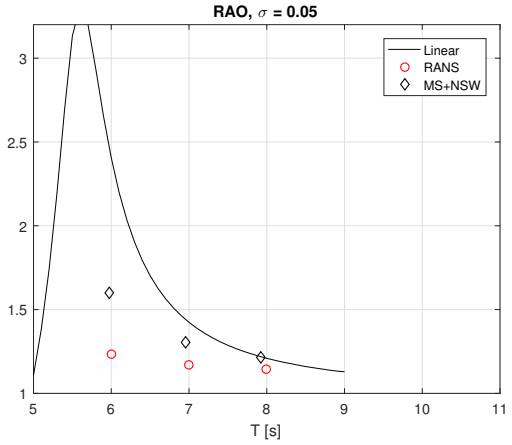

(c) RAO plot for a heaving body

Figure 21: RAO plot for a linear wave of steepness $\sigma = 0.0001$ in figure (a), for a stream wave of steepness $\sigma = 0.025$ in figure (b) and for a stream wave of steepness $\sigma = 0.05$ in figure (c).

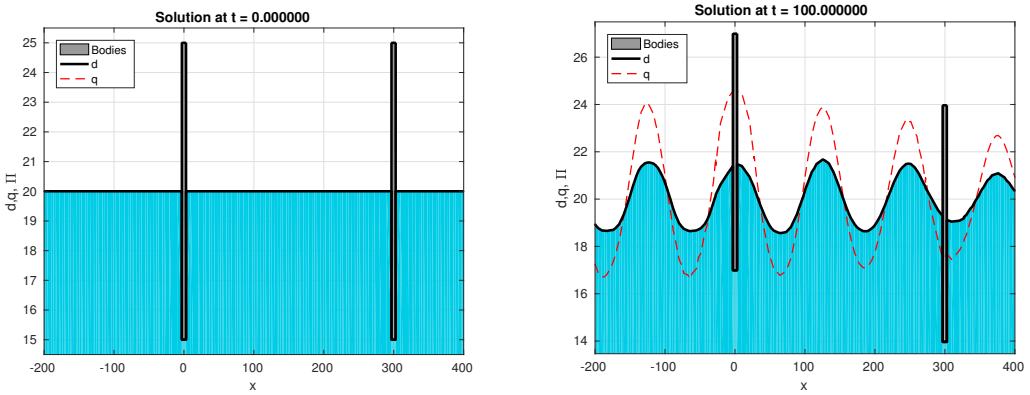

(a) (b)

Figure 22: Multi body problem. Each body can be either a fixed pontoon or a heaving body. In figure (a) the initial set up and in figure (b) the simulation of two heaving bodies with a wave of period $T = 10s$ and steepness $\sigma = 0.025$

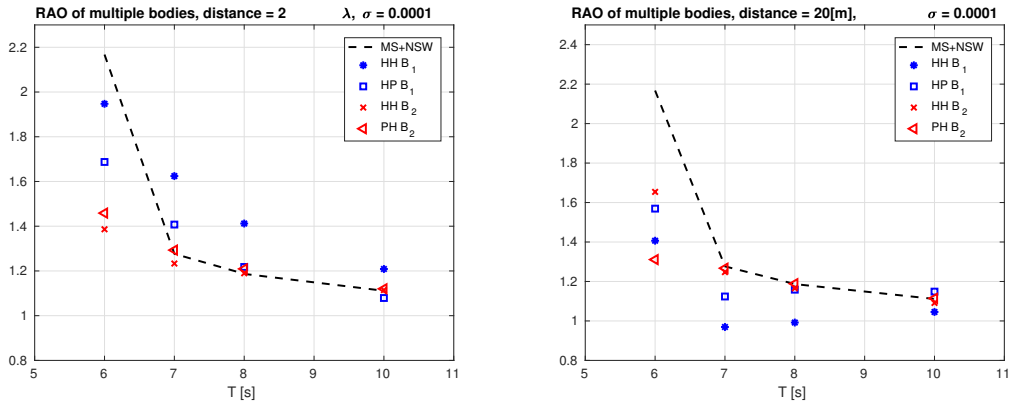

(a) (b)

Figure 23: RAO plots for a stream wave of period $T = [6, 7, 8, 10]s$ and steepness $\sigma = 0.0001$ for the multiple bodies tests with the distance between the bodies dependent on the wave length $l = 2\lambda$ in figure (a) and for a fixed distance of 20 metres in (b): the dashed line is the single body RAO, $*$ and $\times$ the first and second heaving bodies in series, $\square$ a heaving body in front of a pontoon and finally $\triangleleft$, a heaving body behind a pontoon.

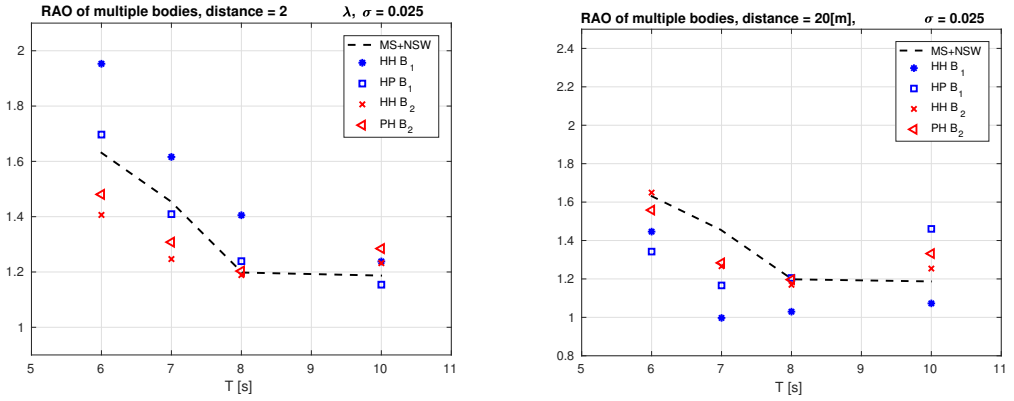

(a) (b)

Figure 24: RAO plots for a stream wave of period $T = [6, 7, 8, 10]s$ and steepness $\sigma = 0.025$ for the multiple bodies testswith the distance between the bodies dependent on the wave length $l = 2\lambda$ in figure (a) and for a fixed distance of 20 metres in (b): the dashed line is the single body RAO, $*$ and $\times$ the first and second heaving bodies in series, $\square$ a heaving body in front of a pontoon and finally $\triangleleft$, a heaving body behind a pontoon.

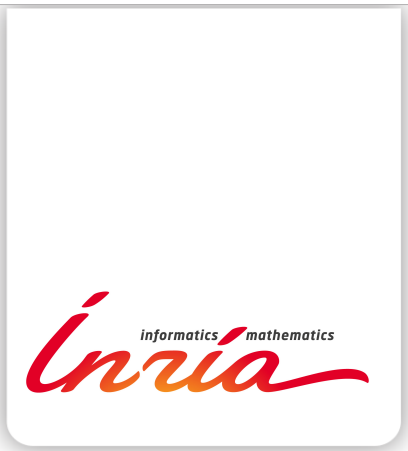

RESEARCH CENTRE
BORDEAUX – SUD-OUEST

200, Avenue de la Vieille Tour
33405 Talence Cedex

Publisher
Inria
Domaine de Voluceau - Rocquencourt
BP 105 - 78153 Le Chesnay Cedex
inria.fr

ISSN 0249-6399